MDPI

Article

Stable boundary layers and subfilter-scale motions

James C. McWilliams[1], Charles Meneveau[2], Edward G. Patton[3] and Peter P. Sullivan[3,*]

[1] Department of Atmospheric and Oceanic Sciences, University of California Los Angeles, CA
[2] Department of Mechanical Engineering, Johns Hopkins University, Baltimore, MD
[3] National Center for Atmospheric Research, Boulder, CO

* Correspondence: pps@ucar.edu

Abstract: Recent high-resolution large-eddy simulations (LES) of a stable atmospheric boundary layer (SBL) with mesh sizes $N = (512^3, 1024^3, 2048^3)$, or mesh spacings $\triangle = (0.78, 0.39, 0.2)$ m, are analyzed. The LES solutions are judged to be converged based on the good collapse of vertical profiles of mean winds, temperature, and low-order turbulence moments, *i.e.,* fluxes and variances, with increasing N. The largest discrepancy is in the stably stratified region above the low-level jet. Subfilter-scale (SFS) motions are extracted from the LES with $N = 2048^3$, and are compared to sonic anemometer fields from the horizontal array turbulence study (HATS) and its sequel over the ocean (OHATS). Results from the simulation and observations are compared using the dimensionless resolution ratio $\Lambda_w/\triangle_f$ where $\triangle_f$ is the filter width and Λ_w is a characteristic scale of the energy containing eddies in vertical velocity. SFS motions from the observations and LES span the ranges $0.1 < \Lambda_w/\triangle_f < 20$ and are in good agreement. The small, medium, and large range of $\Lambda_w/\triangle_f$ correspond to Reynolds Averaged Navier Stokes (RANS), the gray zone (a.k.a. "Terra Incognita" [1]), and fine resolution LES. The gray zone cuts across the peak in the energy spectrum and then flux parameterizations need to be adaptive and account for partially resolved flux but also "stochastic" flux fluctuations that represent the turbulent correlation between the fluctuating rate of strain and SFS flux tensors. LES data with mesh 2048^3 will be made available to the research community through the web and tools provided by the Johns Hopkins University Turbulence Database.

Keywords: stratified turbulence; large-eddy simulation; subfilter scale motions; surface layer observations; gray zone

Citation: McWilliams, J. C.; Meneveau, C.; Patton, E. G.; Sullivan, P. P. Stable boundary layers and subfilter-scale motions. *Atmosphere* **2023**, *1*, 0. https://doi.org/

Received:
Revised:
Accepted:
Published:

1. Preface

Along with others in this collection, this paper is dedicated to our colleague and friend, Jack(son) Herring. It is also an encomium for the long history of turbulence research centered around the National Center for Atmospheric Research (NCAR), where Jack worked from 1972. One of the better purposes of NCAR was as a gathering place for researchers from around the world, especially in the summer outside of teaching terms. Another was as a national supercomputing center beginning even before such a term was invented (*i.e.,* punch cards in the basement of the Mesa Laboratory), and from the outset turbulence simulations were one of the premier scientific applications [*e.g.,* 2]. The summer gatherings were often informal and barely scripted or sometimes formally funded and convened as workshops. They did a great deal to fertilize the development of turbulence theories, simulations, and experiments among the physics, engineering, and geophysical fluid dynamics communities, and to entrain younger scientists into the subject. A conspicuous event was a summer-long school and symposium in 1987 [3]. It was partly managed under the auspices of NCAR's Advanced Study Program, where Jack was first hired, and at some point in the 1980s it was more formally designated as the Geophysical Turbulence

Program (GTP) that continues today. Its scientific scope was broad and its human reach was wide, involving hundreds of scientists whose roster probably no archaeology could recover. Among its luminaries from outside NCAR were R. Kraichnan, U. Frisch, E. Lorenz, D. Montgomery, H. Tennekes, M. Lesieur, and J. Riley, and from within, C. Leith, D. Lilly, J. Deardorff, J. Wyngaard, D. Lenschow, and A. Pouquet; there were many others in and outside NCAR, ourselves, and of course Jack.

2. Introduction

Stratified turbulence impacts many applications and the topic attracts researchers in physics, geophysical, and engineering communities; see reviews [4–7]. The present contribution is narrower in scope focusing on stably stratified turbulent boundary layers (SBLs). The SBL is a key component of earth system modeling, *viz.*, large-scale weather, climate, and ocean models [*e.g.*, 5,6,8–13]. Stratified boundary-layer turbulence is also important in electromagnetic wave propagation in the lower atmosphere, wind energy, and dispersion of pollutants [14–16].

Observations, along with direct numerical simulation (DNS) and large-eddy simulation (LES) are important tools for studying SBLs but each face impediments; simulation results are often at low Reynolds number [17] and require long computational run times, and observations are impacted by inherent atmospheric variability and surface heterogeneity; the latter can result in global impacts on the SBL [18]. Observations and simulations must cope with spatial and temporal intermittency in SBLs with strong stratification [6] and coherent structures [19].

This paper is a report of recent, very high resolution simulations of stable atmospheric boundary layers (SBL) underneath a steady geostrophic wind. It is one of the canonical idealized problems in geophysical fluid dynamics, closely related to Jack's interest in homogeneous stratified turbulence, but with the complication of an adjacent rough, flat boundary. The narrow purpose here is to report on the resolution dependency in LES and make detailed statistical comparisons with near-surface measurements from instrument arrays. A larger goal is to establish the validity of SBL LES as a test-bed for evaluating turbulent closure schemes near the boundary, although we have not yet gone very far in that direction.

The outline of the rest of the paper is the following: §3 presents the LES equations and introduces recent LES of SBLs with fine-mesh resolution; §4 briefly describes field observations collected in the atmospheric surface layer specifically designed to measure subfilter-scale (SFS) fields over a range of atmospheric stability; §5 analyzes the LES solutions and their sensitivity to the mesh resolution, and it compares SFS motions extracted from the LES and field observations, §6 summarizes the findings, and §7 is a brief commentary on the continuing science of turbulence.

3. LES

3.1. Governing equations

The LES model equations for an SBL under the Boussinesq approximation with system rotation and stable stratification with a flat bottom boundary are well documented [*e.g.*, 20,21]. The equations are briefly introduced here:

$$\frac{\partial \overline{\mathbf{u}}}{\partial t} + \overline{\mathbf{u}} \cdot \nabla \overline{\mathbf{u}} = -\mathbf{f} \times (\overline{\mathbf{u}} - \mathbf{U}_g) - \nabla \overline{\pi} + \hat{\mathbf{z}} \beta (\overline{\theta} - \theta_{ref}) - \nabla \cdot \mathbf{T} \tag{1a}$$

$$\frac{\partial \overline{\theta}}{\partial t} + \overline{\mathbf{u}} \cdot \nabla \overline{\theta} = -\nabla \cdot \mathbf{B} \tag{1b}$$

$$\frac{\partial e}{\partial t} + \overline{\mathbf{u}} \cdot \nabla e = \mathcal{P} + \mathcal{B} + \mathcal{D} - \mathcal{E} \tag{1c}$$

$$\nabla \cdot \overline{\mathbf{u}} = 0\,. \tag{1d}$$

The equation set includes transport equations: for momentum $\rho\overline{\mathbf{u}}$ (1a); for virtual potential temperature $\overline{\theta}$ (1b); and for SFS turbulent kinetic energy e (1c). The divergence free (incompressible) condition (1d) determines the elliptic pressure variable $\overline{\pi}$. Variables that appear in (1) are: velocity components $\overline{\mathbf{u}} \equiv \overline{u}_i = (\overline{u}, \overline{v}, \overline{w})$, geostrophic winds $\mathbf{U}_g = (U_g, V_g)$, rotation vector $\mathbf{f} = (0, 0, f)$ with Coriolis parameter f, unit vector $\hat{\mathbf{z}}$ in the vertical direction, and buoyancy parameter $\beta = g/\theta_{ref}$ where g is gravity and θ_{ref} is a reference temperature. Pressure $\overline{p}$ and air density ρ do not appear explicitly in (1). The terms on the right-hand-side of (1c) for e are shear production $\mathcal{P}$, buoyancy production-destruction $\mathcal{B}$, diffusion $\mathcal{D}$, and dissipation $\mathcal{E}$. The modeling of these terms is described in [20]. The overbar notation $\overline{(\,)}$ denotes a spatially filtered quantity.

The LES equations are formally derived by applying a spatial filter term-by-term to the governing equations of motion. This operation introduces the unknown SFS kinematic momentum and temperature fluxes

$$\mathbf{T} \equiv \tau_{ij} = \overline{u_i u_j} - \overline{u}_i \overline{u}_j \quad ; \quad \mathbf{B} \equiv B_i = \overline{u_i \theta} - \overline{u}_i \overline{\theta} \tag{2}$$

For the SBL we adopt the two-part SFS model proposed by Sullivan *et al.* [22] which utilizes the transport equation (1c) and an eddy viscosity approach in the parameterization of the SFS fluxes given by (2). This parameterization is specifically tailored to high-Reynolds number LES that uses rough-wall surface boundary conditions based on Monin-Obukhov (MO) similarity theory. In the eddy viscosity prescription $\nu_t \sim \gamma \sqrt{e}\, \ell$ the isotropy factor $\gamma = S'/(\langle S \rangle + S')$ where $(\langle S \rangle, S')$ are the resolved strain rate average and fluctuation, respectively; the strain rate average is over an x-y plane. The isotropy factor varies with grid resolution and essentially reduces the length scale ℓ as the wall is approached depending on the magnitude of the resolved turbulence fluctuations. The boundary conditions, solution algorithm, and further details are provided in Sullivan *et al.* [21]. To streamline the notation and text in the following discussion, we now drop the overbar symbol on all spatially filtered (*i.e.,* resolved) variables and simply refer to virtual potential temperature θ as "temperature".

3.2. LES of stable boundary layers

The present work targets the LES of the so-called GABLS1 intercomparison case described in detail by Holtslag [23] and Beare *et al.* [24]. The problem design provides an excellent test-bed to study stratified turbulence in a high-Reynolds number boundary-layer flow using LES. GABLS1 is a canonical high-latitude SBL driven by constant geostrophic winds $U_g = 8\,\mathrm{m\,s^{-1}}$ with Coriolis parameter $f = 1.39 \times 10^{-4}\,\mathrm{s^{-1}}$ above a horizontally homogeneous rough surface $z_o = 0.1\,\mathrm{m}$. Simulations are initiated from a neutral state with an overlying stable inversion $\partial_z \theta = 0.01\,\mathrm{K\,m^{-1}}$ imposed at an initial height $z = 100\,\mathrm{m}$. The computational domain size is $(400 \times 400 \times 400)\,\mathrm{m}$. A constant rate of surface cooling $C_r = 0.25\,\mathrm{K\,hr^{-1}}$ is applied starting at $t = 0$ to generate stably-stratified turbulence. The specification of surface temperature fully couples the momentum and temperature relations in the Monin-Obukhov bottom boundary conditions, which is a more demanding test for LES compared to a specified temperature flux: further description of the simulation design are given in Sullivan *et al.* [21]. Previous LES find a quasi-steady SBL featuring a low-level jet with wind profile veering in the SBL after 8 hours of simulation; the SBL depth $h \approx 200\,\mathrm{m}$, the surface temperature flux $Q_* \approx -9\,\mathrm{K\,m\,s^{-1}}$, and friction velocity $u_* \approx 0.25\,\mathrm{m\,s^{-1}}$, which vary with the mesh resolution [21]. The GABLS1 SBL is weakly stable with continuous turbulence, the boundary layer stability metric is $h/L_{mo} \sim 1.7$, where $L_{mo} \approx 118\,\mathrm{m}$ is the Monin-Obukhov length, see Table 1 and definitions of h, L_{mo} in §5.1.

The first GABLS1 intercomparison used LES models with coarse and fine meshes of $N = 128^3$ and 200^3 gridpoints [24,25], suitable to the computational capabilities at that time. Although there was qualitative agreement amongst the LES models, there are hints that increased resolution resulted in shallower SBLs inducing a change in surface friction

Figure 1. Twin horizontal arrays of sonic anemometers used to measure subfilter scale variables in the atmospheric surface in the HATS field campaign. The upper array is located at $z_d = 8.66\,\mathrm{m}$ with anemometer horizontal spacing $\delta y_d = 2.17\,\mathrm{m}$. The vertical location and horizontal spacing of anemometers in the lower array are $(z_s, \delta y_s) = (4.33, 1.08)\,\mathrm{m}$. Photo courtesy of Thomas Horst.

velocity u_* and surface cooling flux Q_*. This motivated further study and Sullivan *et al.* [21] explored the LES solution sensitivity using meshes of $N = (200^3, 512^3, 1024^3)$ grid-points along with four different cooling rates $C_r = (0.25, 0.375, 0.5, 1.0)\,\mathrm{K\,hr^{-1}}$; the 1024^3 simulation required approximately 2 million core hours to complete a 9 hour simulation.

The present work expands on Sullivan *et al.* [21] using an unprecedented resolution of $\triangle = 0.2\,\mathrm{m}$ in all three directions with a mesh of $N = 2048^3$. Because of the computational cost a two-step recipe is used to perform the LES. First, a seed simulation with $N = (512 \times 512 \times 2048)$ is run from scratch for nearly 8 hrs. The grid in this simulation is anisotropic but has the advantage that the wind and temperature profiles vary smoothly in the vertical direction. Next, the last volume from the seed simulation is archived and the field variables are interpolated in the horizontal x-y directions using zero padded Fourier transforms to generate a restart volume with $N = 2048^3$ points. The fine mesh solution is then started and run for an additional 0.5 hr. This simulation strategy results in smooth restarts with the high wavenumber part of the spectrum rapidly filled with small-scale turbulence. Two simulations with weak and strong cooling rates $C_r = (0.25, 1)\,\mathrm{K\,hr^{-1}}$ are carried out.

Selected snapshots from the two simulations as well as time sequences with the 2048^3 mesh are being included as part of datasets available to the community at the Johns Hopkins Turbulence Databases (JHTDB). The system enables scientists access to world-class simulations using the approach of "Immersive Analysis" which allows the user to insert immersive "virtual sensors" into the simulated flow. This approach facilitates access to large datasets without having to download large amounts of data, as well as to perform analysis close to the data [26,27]. The ability to query data in spatially localized fashion is particularly relevant to the SBL whose fields are characterized by strong spatially and temporally intermittent events. At the time of this writing, the data ingest and data publishing process has not yet been finished, but completion is expected soon.

Table 1. Bulk simulation properties, with entries: LES case, mesh points N, cooling rate C_r, mesh spacing $\triangle$, friction velocity u_*, temperature flux Q_*, boundary layer height h, Monin-Obukhov stability length L_{mo}, boundary layer stability h/L_{mo}.

Case	N	C_r (K hr^{-1})	$\triangle$ (m)	u_* (m s^{-1})	$Q_* \times 10^3$ (K m s^{-1})	h (m)	L_{mo} (m)	h/L_{mo}
B	512^3	0.25	0.78	0.265	-10.5	205.3	119.3	1.72
C	1024^3	0.25	0.39	0.255	-9.63	197.5	116.4	1.70
C2	2048^3	0.25	0.20	0.249	-8.83	187.2	118.6	1.56
F2	2048^3	1.0	0.20	0.177	-14.82	143.7	24.9	5.77

4. Observations of subfilter-scale motions

An alternative to using low-Reynolds number DNS datasets for *a priori* tests [28] of SFS models is to use laboratory measurements of higher Reynolds number turbulence collected at multiple spatial points. In principle, measurement data can then be spatially filtered mimicking the spatial filtering operation in LES [29]. At still higher Reynolds numbers a similar approach can be undertaken using measurements in the atmospheric surface layer. The latter was frequently championed in seminars and discussions with John Wyngaard when visiting NCAR. The horizontal array turbulence study (HATS) was a field campaign [30] specifically designed to construct SFS motions from turbulence data collected at multiple locations in the atmospheric surface layer over a range of stability. HATS, carried out in the central California valley, was a collaborative community effort between NCAR and GTP, Johns Hopkins University, Pennsylvania State University, and Clemson University. The field campaign built on work by several groups including Meneveau and Lund [31], Tong *et al.* [32,33], Tao *et al.* [34]; see the many cited references in these papers and the review [35].

HATS used two horizontal crosswind arrays of sonic anemometers mounted at different vertical locations as shown in Fig. 1; four array configurations varying the sonic anemometer horizontal separation and vertical location were used in HATS. The anemometer arrays measured time series of the turbulent velocity components (u, v, w), (streamwise, crosswind, vertical) and virtual potential temperature θ. The multi-point measurements in the crosswind direction y are combined with Taylor's frozen field assumption in the streamwise direction x [*e.g.*, 36] to create x-y planes of stratified turbulence $(\mathbf{u}, \theta)(x, y, z, t)$. Wind speed and diurnal variations combined with spatial variations in the instrument positioning created a rich dataset for studying spatially filtered turbulence in the atmospheric surface layer. For example, Wyngaard [1], Sullivan *et al.* [37], Kleissl *et al.* [38,39], Chen and Tong [40], Hatlee and Wyngaard [41], Chamecki *et al.* [42], Ramachandran and Wyngaard [43] studied SFS dynamics, evaluated eddy viscosity models, dynamic Smagorinsky models, subfilter-scale budgets, and rate-equation models using HATS data; the studies employed single and double filtering available from the HATS arrays. Triple filtering was explored in Higgins *et al.* [44] using a 4x4 array of sonic anemometers that enabled also vertical (albeit more sparsely sampled) filtering confirming the accuracy of double filtering. Kumar *et al.* [45] reproduced HATS conditions during a daily cycle using low-resolution LES. The success of HATS motivated follow-on campaigns focused on atmospheric turbulence in the surface layer; over the ocean OHATS [46], over a glacier SnoHATS [47], in an orchard canopy CHATS [48], and over land accounting for horizontal advection AHATS [49].

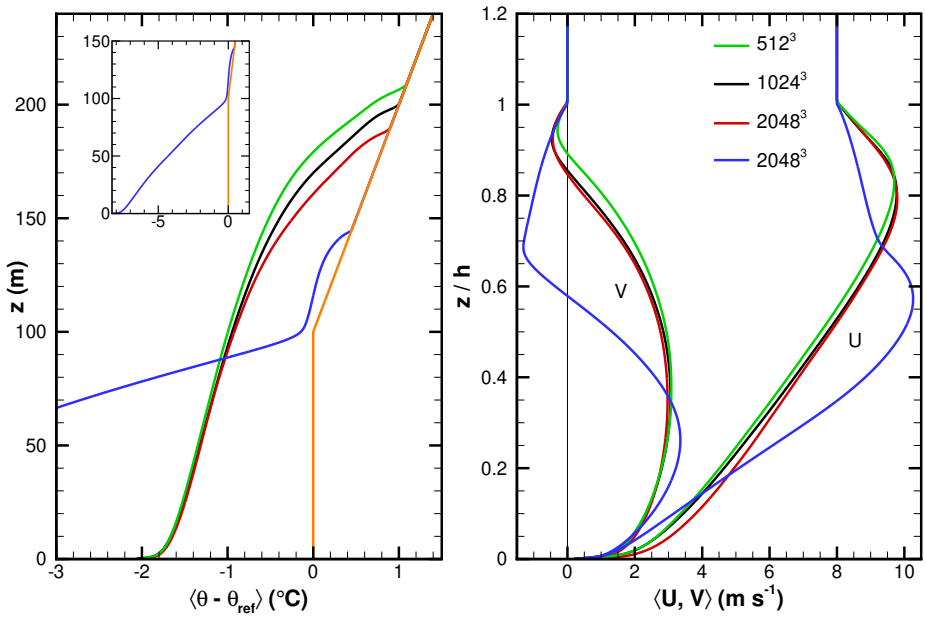

Figure 2. Vertical profiles of average temperature $\langle \theta - \theta_{ref} \rangle$ left panel. Simulations (B, C, C2) with cooling rate $C_r = 0.25\,\mathrm{K\,hr^{-1}}$ and $N = (512^3, 1024^3, 2048^3)$ line colors (green, black, red), respectively. Simulation F2 with $C_r = 1\,\mathrm{K\,hr^{-1}}$ and $N = 2048^3$ indicated by blue line color. The inset figure shows the variation of temperature in F2 in the lower SBL. The initial temperature field at $t = 0$ is shown as the orange line and $\theta_{ref} = 265\,\mathrm{K}$. Vertical profiles of average winds $\langle U, V \rangle$ are shown in the right panel. Note the vertical coordinate for the wind profiles is normalized by the SBL height h from each simulation.

5. Results

5.1. SBL low-order moments

The advent of high performance computing allows mesh convergence to be studied using 3D simulations. Solution convergence in LES is complicated by the mesh dependence in the SFS model, *e.g.*, holding the domain size fixed the resolved flux in a 100^3 simulation is of course different than the resolved flux in a 2048^3 simulation. Judging convergence in LES is also challenging as the subgrid-scale model and numerical discretization errors are intertwined since both depend explicitly on the mesh spacing [50]. Here we use physically based metrics based on vertical profiles of low-order statistical moments to judge convergence as discussed in Sullivan and Patton [51] for convectively driven boundary layers, also see Geurts and Fröhlich [52]. Table 1 provides a summary of bulk parameters for SBL simulations with $C_r = 0.25\,\mathrm{k\,hr^{-1}}$ and grid meshes $N = (512^3, 1024^3, 2048^3)$ and $C_r = 1\,\mathrm{K\,hr^{-1}}$ and $N = 2048^3$. Variables in Table 1 are: LES case, grid mesh points N, mesh spacing $\triangle$, cooling rate C_r, friction velocity u_*, surface temperature flux Q_*, boundary layer depth h, Monin-Obukhov stability length $L_{mo} = -u_*^3/\kappa\beta Q_*$ with von Kármán constant $\kappa = 0.4$, and boundary layer stability h/L_{mo}. The SBL depth h is defined as the vertical location where the vertical gradient of temperature $\partial_z\langle\theta\rangle$ reaches a maximum, see [21,53]. There is variation in (u_*, Q_*) with grid resolution because of variability in the SBL depth h. Dai *et al.* [54] speculates this is a consequence of the stability length scale correction used in the LES. Statistics, denoted by angle brackets $\langle\,\rangle$, are formed by averaging in x-y planes and over the time period $8 < t < 9\,\mathrm{hr}$, except for simulation C2 which used a shorter 30 minute time average. A turbulent fluctuation from a horizontal mean is denoted by a superscript prime $(\,)'$.

Figure 2 compares profiles of winds and temperature for 3 different resolutions $(512^3, 1024^3, 2048^3)$ with fixed surface cooling $C_r = 0.25\,\mathrm{K\,hr^{-1}}$. To eliminate the slight

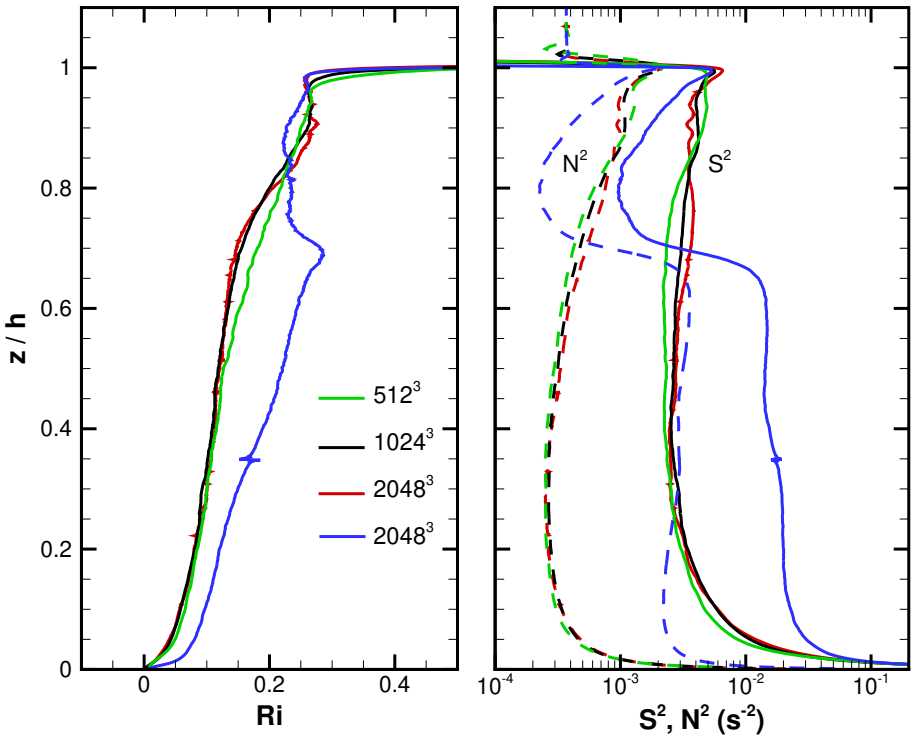

Figure 3. Vertical profiles of average Richardson number left panel. Simulations with cooling rate $C_r = 0.25\,\mathrm{K\,hr^{-1}}$ (B, C, C2) with $N = (512^3, 1024^3, 2048^3)$ indicated by line colors (green, black, red), respectively. Simulation F2 with $C_r = 1\,\mathrm{K\,hr^{-1}}$ and $N = 2048^3$ indicated by blue line color. Vertical profiles of average shear and buoyancy frequency squared (S^2, N^2), indicated by (solid, dashed) lines, respectively, are shown in the right panel.

variability with boundary layer depth we introduce the dimensionless vertical coordinate z/h as shown in the right panel of Fig. 2. The flux and variance profiles are normalized by surface values (u_*^2, Q_*) as appropriate. Under this normalization the wind profiles collapse well (the right panel of Fig. 2). The low level jet is positioned at $z/h = 0.8$ and its magnitude is $1.2U_g$.

Vertical profiles of the Richardson number Ri and the squared shear and buoyancy frequency (S^2, N^2) are displayed in Fig. 3 for the three resolutions considered. Here

$$Ri(z) = \frac{N^2}{S^2} \;;\; N^2 = \frac{g}{\theta_{ref}}\frac{\partial\langle\theta\rangle}{\partial z} \;;\; S^2 = \left(\frac{\partial\langle\mathbf{u}_\perp\rangle}{\partial z}\right)^2. \tag{3}$$

where the horizontal wind aligned with the mean wind direction is given by $u_h = \mathbf{u}_\perp(\mathbf{x}, t) \cdot \langle\mathbf{u}_\perp\rangle/|\langle\mathbf{u}_\perp\rangle|$. The profiles of (Ri, S^2, N^2) are very well converged for the three different mesh resolutions below $z/h < 0.5$. In the upper SBL, above the low level jet the profiles for simulations C2 and C are converged. These profiles show that the simulation is in the weakly stable regime as in Sullivan *et al.* [21]. In particular, the profile $Ri(z) \approx 0.2$ shows the approximate validity of the very simple RANS parameterization of a constant Richardson number above the Monin-Obukhov surface layer.

Figures 2 and 3 also illustrate a strong dependence on bulk stratification in the SBL. The bulk stability measure h/L_{mo} increases from 1.56 to 5.77 as the cooling rate varies from $C_r = 0.25$ to $1\,\mathrm{K\,hr^{-1}}$. Increasing stratification leads to a decrease in SBL turbulence level and as a result the height of the low level jet (LLJ) descends from $z/h = 0.8$ to 0.58, *i.e.*, from 105 m to 83 m. Then the wind veering in F2 is sharper and compressed in the lower SBL compared to C2. In F2, notice the SBL is nearly equally split between vertical layers below

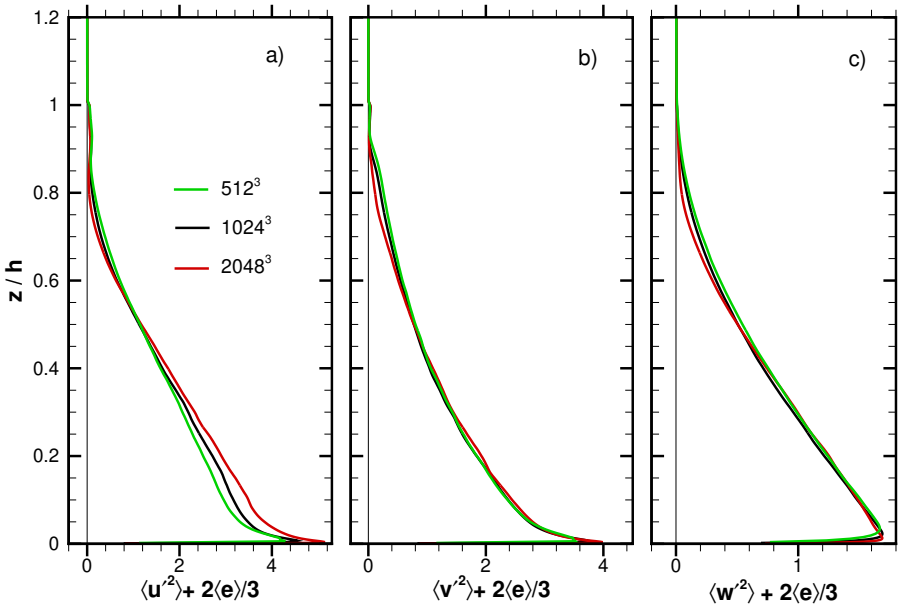

Figure 4. Vertical profiles of velocity variances $\langle u'^2, v'^2, w'^2 \rangle / u_*^2$ panels a), b), c), respectively. The variances include an estimate of the SFS contribution $2\langle e \rangle /3$. Results are from simulations (B, C, C2) with $N = (512^3, 1024^3, 2048^3)$ indicated by line colors (green, black, red), respectively. The vertical coordinate is normalized by the SBL height h from each simulation.

and above the LLJ. The mean wind, temperature, shear, and buoyancy profiles all change markedly above the LLJ compared to their counterparts in the lower SBL. Compensating changes in the shear and buoyancy profiles lead to a relatively uniform $Ri \sim 0.2$ profile above the LLJ which supports weak stratified turbulence. A further discussion of the impacts of increasing stratification on SBL statistics is given in [21].

The velocity variances from simulations (B, C, C2), which include the SFS contribution $2\langle e \rangle /3$, collapse reasonably well for the three mesh resolutions considered as shown in Fig. 4. The momentum and temperature fluxes $\langle u'w', v'w', w'\theta' \rangle$ that include both resolved and SFS contributions are in close agreement as the mesh spacing varies from $\triangle = (0.78, 0.39, 0.20)$; see Fig. 5. The profile of SFS energy $\langle e \rangle$, shown in Fig. 6, shows a systematic decrease with resolution over the bulk of the SBL. For example, at $z/h = 0.5$ the scaling relationship $e \propto \triangle^{2/3}$ holds [36, p. 589]. The results in Fig. 6 find a 40% decrease in e for a mesh-size reduction from 0.78 m to 0.2 m. Based on these results, we judge the LES results to be well converged.

5.2. Structures in stable boundary layers

Flow visualization is extensively utilized to identify turbulent structures in the SBL, an example is provided in Fig. 7. This image shows instantaneous temperature isolines in an x-z plane from simulations C2 and F2 with weak and strong stratification, respectively. Inspection of the images shows an abundance of tightly compressed contour lines sprinkled throughout the SBL, the sharp gradients in θ are signatures of warm-cold temperature fronts passing through the domain. Notice the temperature fronts are very sharp and tilted in the downstream direction, primarily a consequence of the sheared streamwise velocity $\langle u \rangle (z)$. Animations show the spatial and temporal evolution of the fronts (not shown). Frequently the fronts are observed to extend over the full depth of the SBL and nearly the full horizontal extent of the domain as shown in the upper panel of Fig. 7. Turbulent mixing between fronts at different z levels leaves voids with nearly constant temperature. Thus at a fixed x-y location a vertical profile of θ displays a staircase pattern as different front families are crossed. As the stratification increases, the fronts tilt farther downstream and

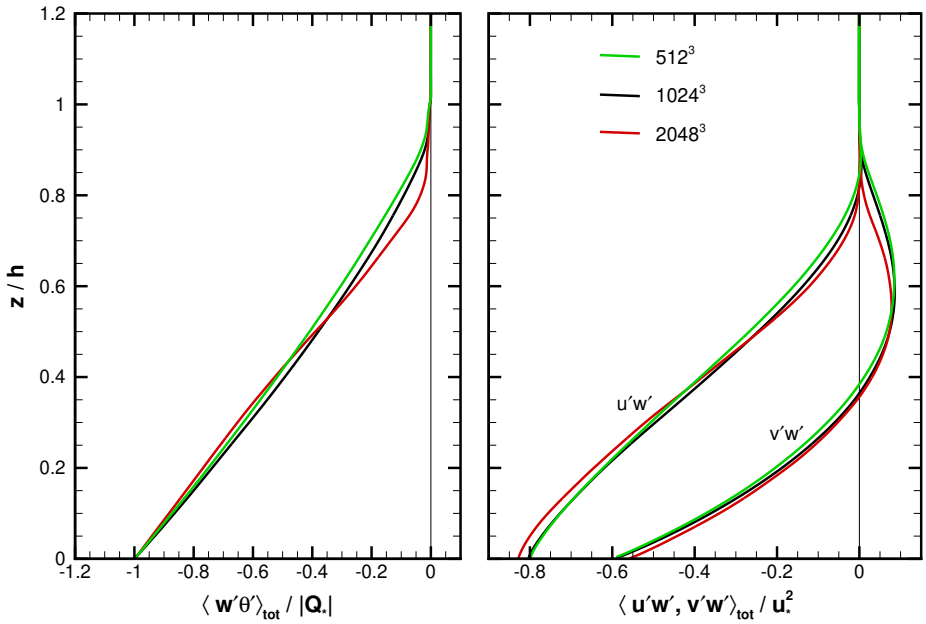

Figure 5. Vertical profiles of average temperature flux (left panel) and momentum fluxes (right panel). The fluxes are normalized by Q_* and u_*^2 as appropriate. The fluxes include the SFS contributions. Results are from simulations (B, C, C2) with $N = (512^3, 1024^3, 2048^3)$ indicated by line colors (green, black, red), respectively. The vertical coordinate is normalized by the SBL height h from each simulation.

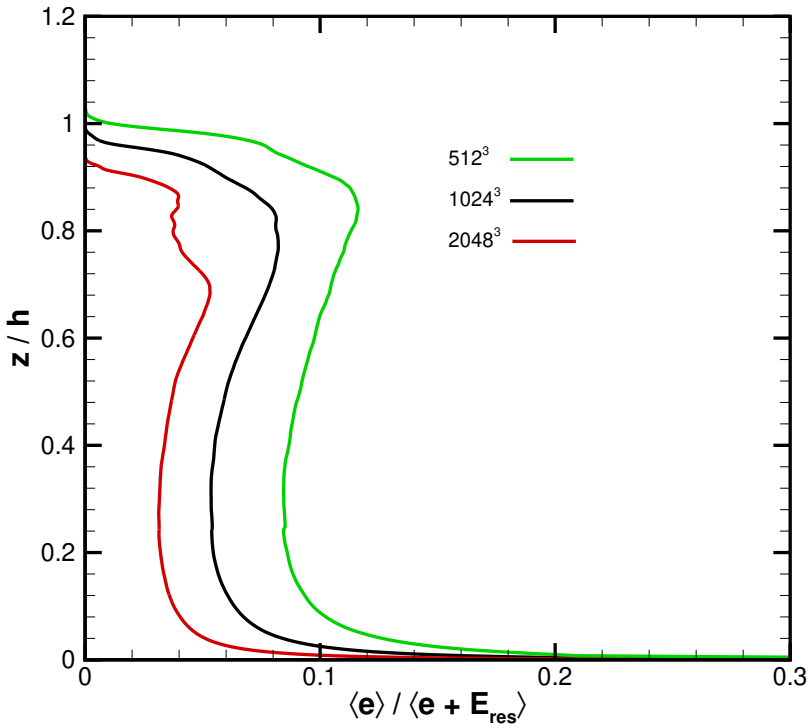

Figure 6. Vertical profile of SFS energy in the LES as fraction of the total energy $\langle e \rangle / \langle e + E_{res} \rangle$ for different meshes $N = (512^3, 1024^3, 2048^3)$ denoted by (green, black, red) lines. The resolved kinetic energy $E_{res} = (u'^2 + v'^2 + w'^2)/2$.

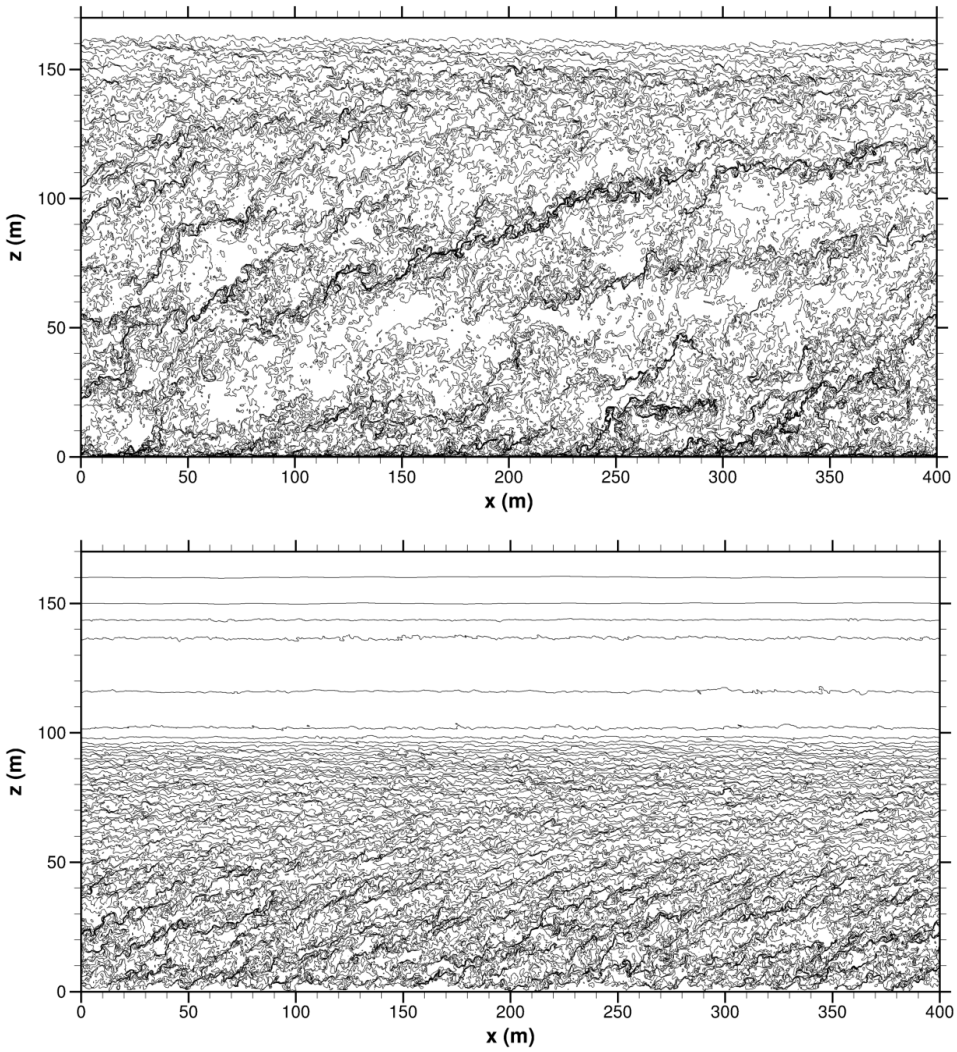

Figure 7. Temperature isolines in an x-z plane from simulations with weak surface cooling (C2 upper panel) and strong surface cooling (F2 lower panel) at $t \sim (8.556, 8.352)$ hr, respectively. In the upper panel there are 51 contour levels between $(-2 < \theta - \theta_{ref} < 0)^{\circ}$C. In the lower panel there are 71 contour levels between $(-7.5 < \theta - \theta_{ref} < 0)^{\circ}$C. In addition, in the lower panel contour levels $(0.2, 0.4, 0.5, 0.6)^{\circ}$C are shown for $z > 135$ m. The reference temperature $\theta_{ref} = 265$ K.

the separation between fronts shrinks considerably as shown in the lower panel of Fig. 7. A horizontal slice through the domain at $z/L_{mo} = 0.164$ m from simulation C2 provides a sense of the front coherence in the spanwise direction as well as the spatial randomness of the fronts. Figure 8 shows multiple fronts at various positions in the horizontal domain, the spanwise extent of a front is ~ 50 m or less. At this instance in the simulation the warm upstream side of the front is modestly stronger than the cool downstream side of the front.

Linear stochastic estimation (LSE) pioneered by Adrian [55] is used to compute conditional averages of the turbulent fields in the SBL. Our application of LSE [21] uses an event trigger based on a positive-negative temperature jump separated by a finite distance in a horizontal plane. This event choice is guided by the instantaneous flow visualization of θ' shown in Fig. 8 which depicts numerous warm-cool temperature fronts. As an example, our LSE temperature event with $E = \pm 0.1$ K corresponds to a scalar flux about 5 times the surface value $|Q_*|$. Conditional fields $(\widehat{\mathbf{u}}, \widehat{p}, \widehat{\theta})$, velocity gradient tensor $\partial_j \widehat{u}_i$, and vorticity $\nabla \times \widehat{\mathbf{u}}$ are estimated for a range of vertical locations, spatial separation, and event

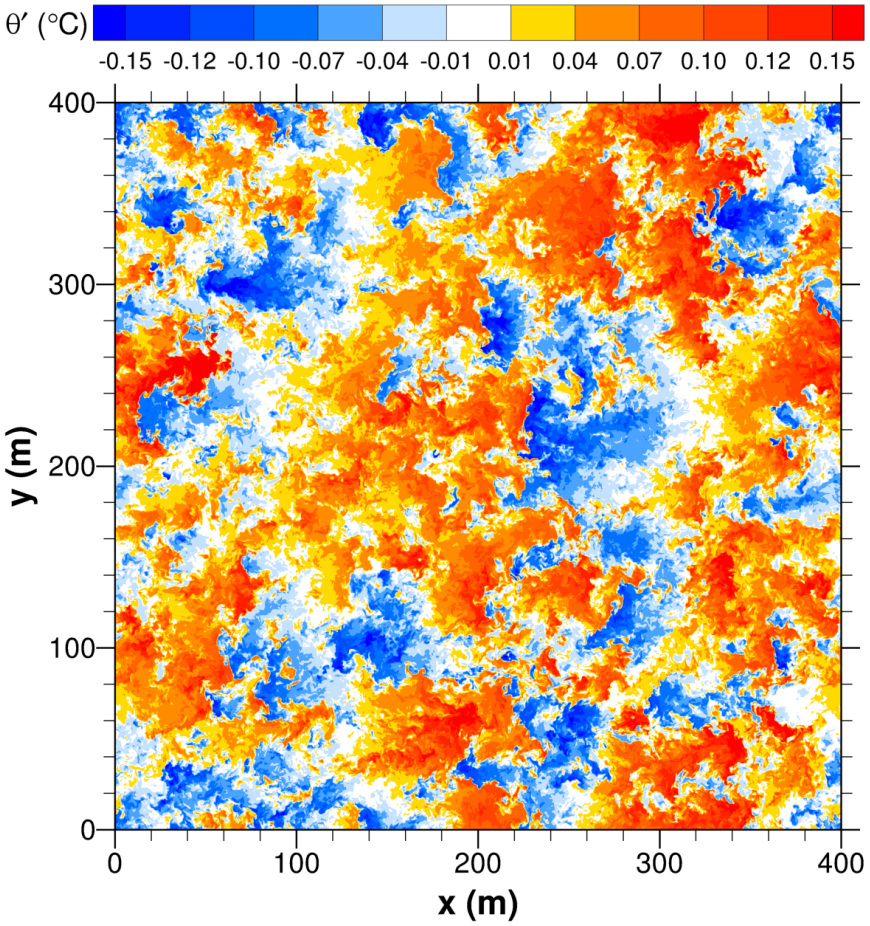

Figure 8. Fluctuating temperature field θ' at $z/L_{mo} = 0.164$ from simulation C2 at $t = 8.556$ hr. Examples of sharp warm-cold temperature fronts are located at $(x, y) = (20, 230), (200, 270), (230, 50), (230, 220), (330, 340)$ m. The color bar for $\theta' = \theta - \langle\theta\rangle$ is in units of °C.

amplitudes [21]. Our conditional sampling finds pairs of counter-rotating vortices in the SBL as shown in Fig. 9. The vortices are aligned with the mean wind direction and are tilted forward in the downstream direction. The upstream vortices act in concert to pump warm fluid forward while the downstream vortices pump cool fluid backwards resulting in a near stagnation point in the region between the vortices. The front boundary is very sharp but the vortices creating the fronts are well resolved coherent structures. Sullivan *et al.* [21] shows the scale of the vortices lies near the peak in the spectrum for θ and w. The coherent structures in the interior of a sheared SBL are considerably different than the pancake vortices in large-scale stably stratified turbulence away from a boundary [*e.g.*, 56].

5.3. SFS motions in observations and LES

The HATS dataset contains a mix of variations in wind speed, stratification and perturbations in the array configuration, *i.e.*, the vertical location z_d and horizontal separation δy_d of the anemometers shown in Fig 1. To account for these variations in computing the SFS motions Sullivan *et al.* [37] introduced a resolution ratio $\Lambda_w/\triangle_f$. The filter scale $\triangle_f \propto \delta y_d$ and is isotropic in x-y, only 2D filtering is employed in HATS. Vertical velocity is used to define Λ_w for the following reasons; w is the least resolved field in LES, w statistics closely follow Monin-Obukhov similarity relationships in the surface layer, and w impacts vertical fluxes which are key ingredients in LES and also large scale models. The length scale $\Lambda_w = 2\pi\langle U\rangle\tau_p$ where $\langle U\rangle$ is the mean wind speed and τ_p is the Eulerian integral time scale for vertical velocity. The autocorrelation function for w is fit to the

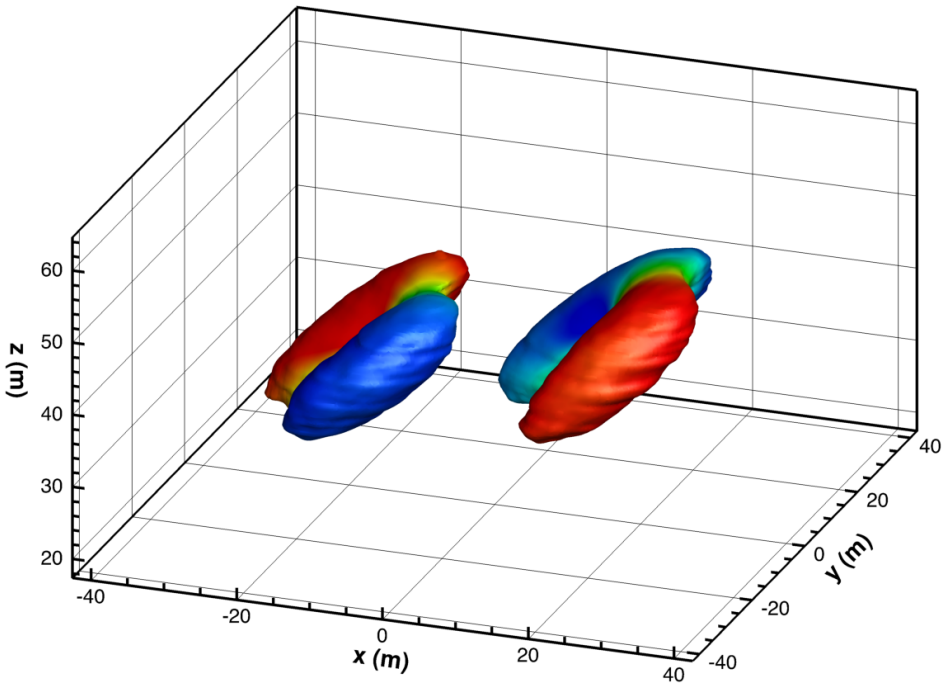

Figure 9. Oblique view of the typical 3D vortical structures in the SBL at a height $z/z_i = 0.2$ from simulation C with grid mesh 1024^3 points [21] obtained using linear stochastic estimation-based conditional averaging. To indicate the sign of vortical rotation, the surface is colored by the vertical component of the vorticity vector $\zeta\,\hat{\mathbf{z}}$ with deep red (blue) colors corresponding to positive-upward (negative-downward) rotation, respectively. The mean horizontal winds are from left to right and at this height turn 30.6 degrees towards the $+y$ direction.

form $R_w(t) = \exp(-t/\tau_p)$. This equates to finding a spectral peak in the vertical velocity spectrum assuming a high wavenumber spectrum k^{-2} see Kaimal and Finnigan [57, p. 63], Sullivan *et al.* [37] and Horst *et al.* [30]. This definition of Λ_w is robust and accounts for distance z above the surface and stratification. In HATS the resolution ratio spans the range $0.1 < \Lambda_w/\triangle_f < 10$.

Physically, $\Lambda_w/\triangle_f$ is a measure of the scale separation between the large-scale energy containing eddies and eddies near the filter scale as sketched in Fig. 10. For $\Lambda_w/\triangle_f \gg 1$ the separation is wide and the turbulence is well resolved with the filter scale in the inertial range. Meanwhile for $\Lambda_w/\triangle_f \leq 1$ the filter scale is near or left of the energy containing eddies and the energy containing turbulence is thus under resolved. The ratio $\Lambda_w/\triangle_f$ is a measure of the simulation resolving power. When $\Lambda_w/\triangle_f \gg 1$ the simulation is LES and when $\Lambda_w/\triangle_f \ll 1$ the simulation is akin to unsteady Reynolds-Averaged Navier Stokes (RANS). Wyngaard [1] calls the intermediate regime $\Lambda_w/\triangle_f \sim 1$ "Terra Incognita" which has similarity with the so-called gray zone [*e.g.*, 58,59]; it's unknown if SFS closures used in LES or RANS are applicable in the gray zone. As $\Lambda_w/\triangle_f$ varies between the LES and RANS limits the length scale ℓ in an eddy viscosity closure is predicted to vary linearly with the grid spacing $\ell \propto \min(\triangle, \ell_t)$ until $\triangle$ exceeds the scale of the energy containing eddies ℓ_t, then ℓ becomes constant [60]. The crossover from LES to RANS is also recognized in the engineering community, Perot and Gadebusch [61] describe a two-equation self adapting closure that spans the regime from DNS to LES to RANS for a mixing layer. Our estimate of a scale-aware length scale for dissipation in the SBL is discussed below.

To make a quantitative comparison between HATS and LES, we define the LES length scale Λ_w in terms of the spatial autocorrelation of vertical velocity $R_w(x, y)$, but aligned with the mean wind direction see Fig. 11. For LES, $\Lambda_w = 2\pi L_w$ where L_w is the integral scale obtained by integration of the autocorrelation $R_w(x', y' = 0)$ from $x' = 0$ to its first-

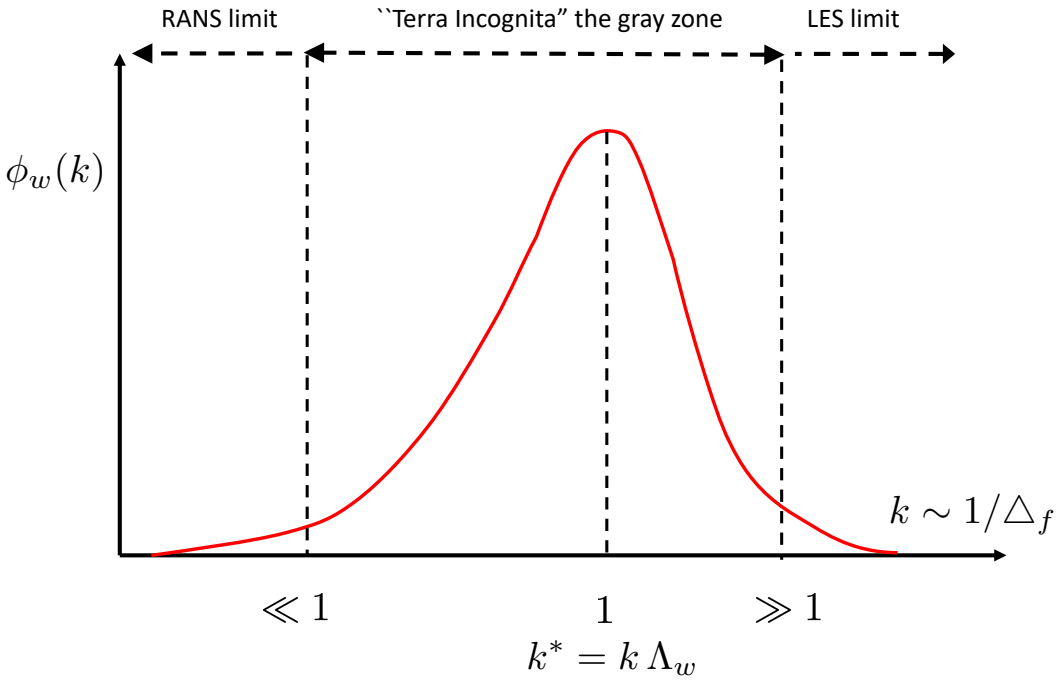

Figure 10. A sketch of the vertical velocity spectrum $\phi_w(k)$ in a horizontal plane as function of the horizontal wavenumber magnitude k. Its peak is at the non-dimensional wavenumber $k^* = k\,\Lambda_w = \Lambda_w/\triangle_f = 1$. The limits $k^* = \Lambda_w/\triangle_f \gg 1$ and $k^* = \Lambda_w/\triangle_f \ll 1$ are the LES and RANS regimes respectively. In between these two limits is "Terra Incognita" or the gray zone. Figure is adapted from Wyngaard [1].

zero crossing; Taylor's hypothesis is not used. The resolved fields $(\mathbf{u}, \theta)$, used to compute SFS motions, are also rotated into the mean-wind coordinate frame (x', y').

Analysis of the LES fields uses a filter scale $\triangle_f$ referenced to the scale $\triangle_c$ used in its subgrid model. For simulation C2 with the 2048^3 mesh and uniform spacing in all three directions the length scale in the subgrid model is $\triangle_c = (9/4)^{1/3}\triangle = 0.25\,\text{m}$. Filter scales in the range $5 < \triangle_f/\triangle_c < 1000$ are used in the present analysis. The lower limit is chosen to help minimize contamination from the subgrid model while the upper limit is constrained by the horizontal dimensions of the LES box, 400 m in each direction. Turbulent fields at vertical levels $z/L_{mo} = (0.083, 0.164)$ inside and near the top of the surface layer are analyzed; at these two levels $\Lambda_w = (21.1, 26.7)\,\text{m}$. Thus, the resolution ratio possible with the LES data spans $0.1 < \Lambda_w/\triangle_f < 20$ which nicely overlaps with the HATS data. The spatial filtering is a simple top-hat filter applied sequentially in the x-y directions, and results from 10 volumes are averaged to construct the SFS statistics. The SFS momentum and temperature fluxes, in both observations and LES, are constructed from:

$$\tau_{ij} \;=\; \widehat{u_i u_j} - \widehat{u}_i \widehat{u}_j \quad \text{and} \quad \tau_{i\theta} \;=\; \widehat{u_i \theta} - \widehat{u}_i \widehat{\theta}\,, \tag{4}$$

where the overhat notation $\widehat{(\;)}$ denotes two-dimensional x-y spatial filtering at $\triangle_f$.

The variation of SFS velocity variances $\langle \tau_{11}, \tau_{22}, \tau_{33} \rangle$, momentum fluxes $\langle \tau_{12}, \tau_{13} \rangle$, and temperature fluxes $\langle \tau_{1\theta}, \tau_{3\theta} \rangle$ with varying resolution ratio $\Lambda_w/\triangle_f$ from HATS, OHATS and LES are shown in Figs. 12, 13, and 14, respectively. Because of physical constraints OHATS employed only a single array with horizontal spacing $\delta y_d = 0.58\,\text{m}$. As a result, the variation in $\Lambda_w/\triangle_f$ from OHATS is a consequence of weak diurnal changes and possible wave effects over the ocean. The small value of $\triangle_f$ pushes all the OHATS results towards large $\Lambda_w/\triangle_f \sim 6$ to 10. HATS employed four different array configurations and coupled with a vigorous diurnal cycle results in a wide range of the resolution ratio. Inspection of the HATS data shows stratification is important as the spectral peak in vertical velocity

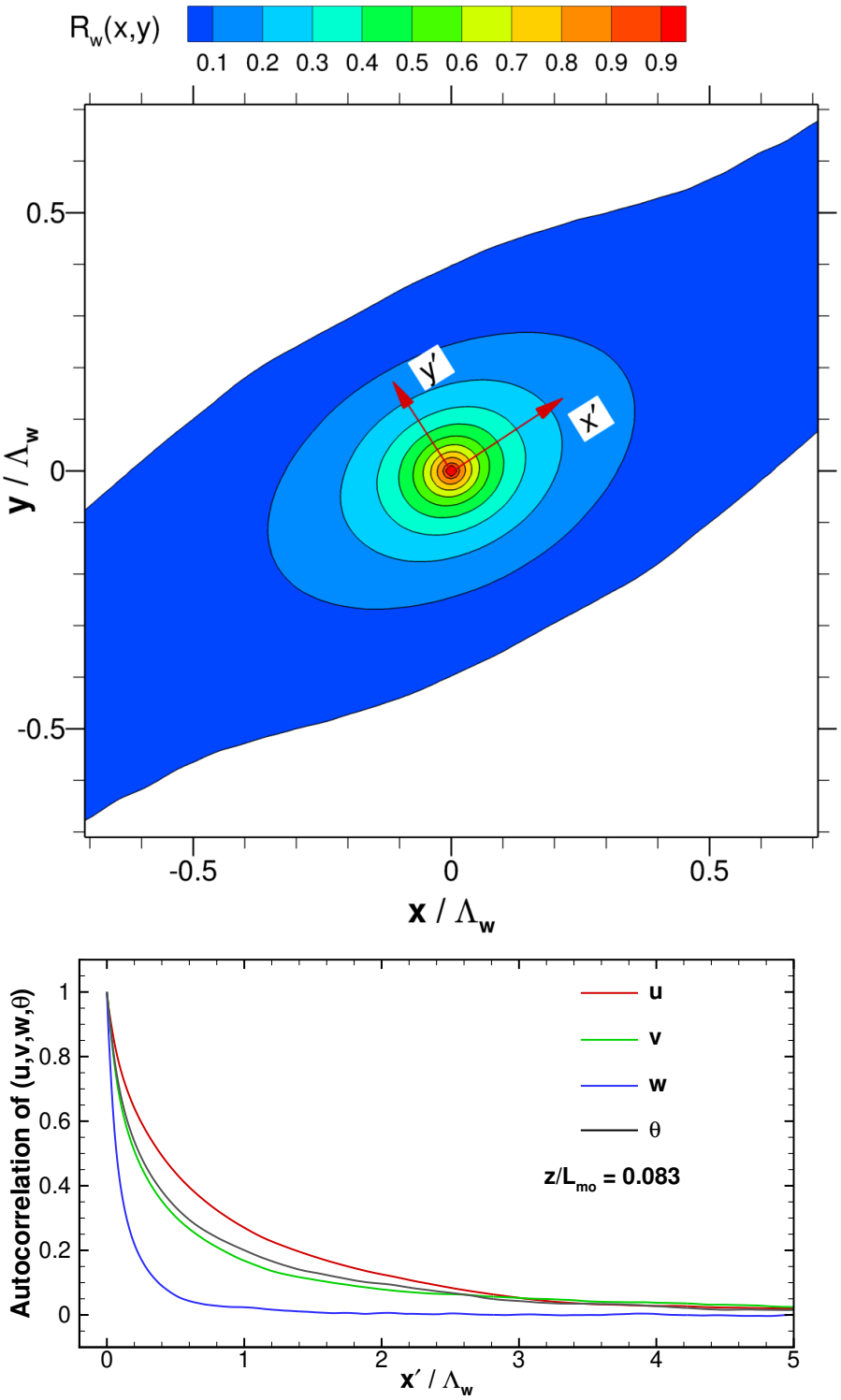

Figure 11. Two dimensional autocorrelation for vertical velocity $R_{ww}(x, y)$ at $z/L_{mo} = 0.083$ from simulation C2 at $t = 8.556$ hr (upper panel). The 1d correlation, extracted from the 2d correlation, for (u, v, w, θ) aligned with the mean wind direction x' at $y' = 0$ (lower panel). The peak wavelength for the w correlation is $\Lambda_w = 21.0$ m.

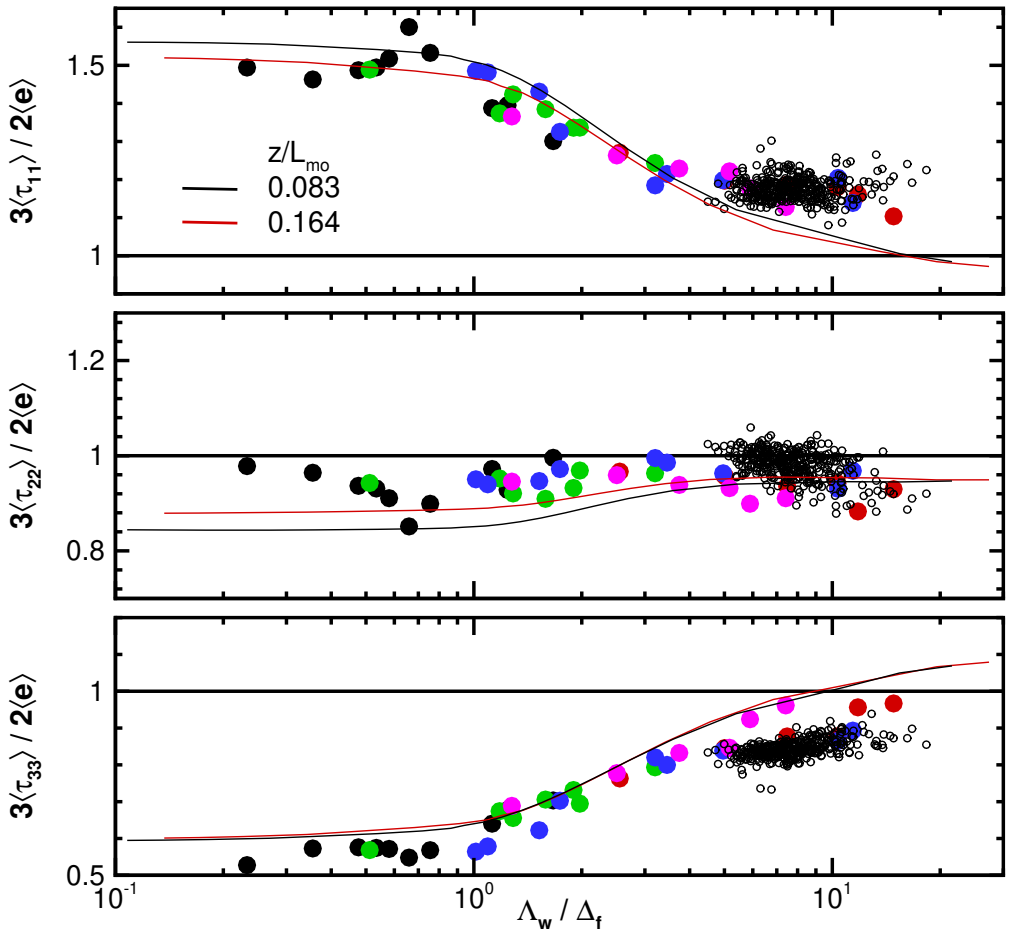

Figure 12. Variation of subfilter-scale velocity variances with resolution ratio $\Lambda_w/\triangle_f$. Measurements are collected in the atmospheric surface layer over land (colored bullets are from different sonic arrays in HATS) and over the ocean (open circles from OHATS) [37,46]. The (red, black) lines are filtered results from simulation C2 with mesh 2048^3. The (red, black) lines are in the surface layer $z/L_{mo} = (0.164, 0.083)$ respectively. The measurements and simulation results highlight the deviation from isotropy when the resolution ratio is $\Lambda_w/\triangle_f \sim \mathcal{O}(1)$.

shifts from large to small scales as the stratification transitions from unstable to stable [57]. For example, results from HATS array-1 at $z_d = 4.18$ m, blue bullets in Fig. 12, span nearly a decade in $\Lambda_w/\triangle_f$ as $-0.3 < z_d/L_{mo} < 1.6$ see Sullivan *et al.* [37].

Overall the qualitative agreement between the simulation results and observations for variances and fluxes is good, and in some instances the comparison is quantitatively good. The normal variances τ_{ii} in Fig. 12 are essentially a bulk metric of SFS isotropy. Observations and simulations both show the variances $\langle\tau_{ii}\rangle$ tend to unity only for large $\Lambda_w/\triangle_f \geq 10$; isotropy at small scales is an implicit assumption in most Smagorinsky closures for LES, and thus fine computational grids are apparently needed to satisfy this metric. For $\Lambda_w/\triangle_f \leq 1$ the ratio $\langle\tau_{11}\rangle/\langle\tau_{33}\rangle > 2.3$ indicates high anisotropy in the peak energy containing eddies in the streamwise and vertical components. The momentum fluxes $\langle\tau_{12}, \tau_{13}\rangle$ computed from LES fields are in good agreement with the observations. Notice the vertical momentum flux shows an expected steady approach towards $-u_*^2$ at small $\Lambda_w/\triangle_f$ at the level $z/L_{mo} = 0.083$. The results also suggest that the $z/L_{mo} = 0.164$ level is slightly outside the surface layer in the SBL. At small values of $\Lambda_w/\triangle_f \leq 0.4$, LES results show departure of the horizontal variance $\langle\tau_{22}\rangle$ from isotropy, qualitatively consistent with the measurements but perhaps to a somewhat greater degree. The LES also

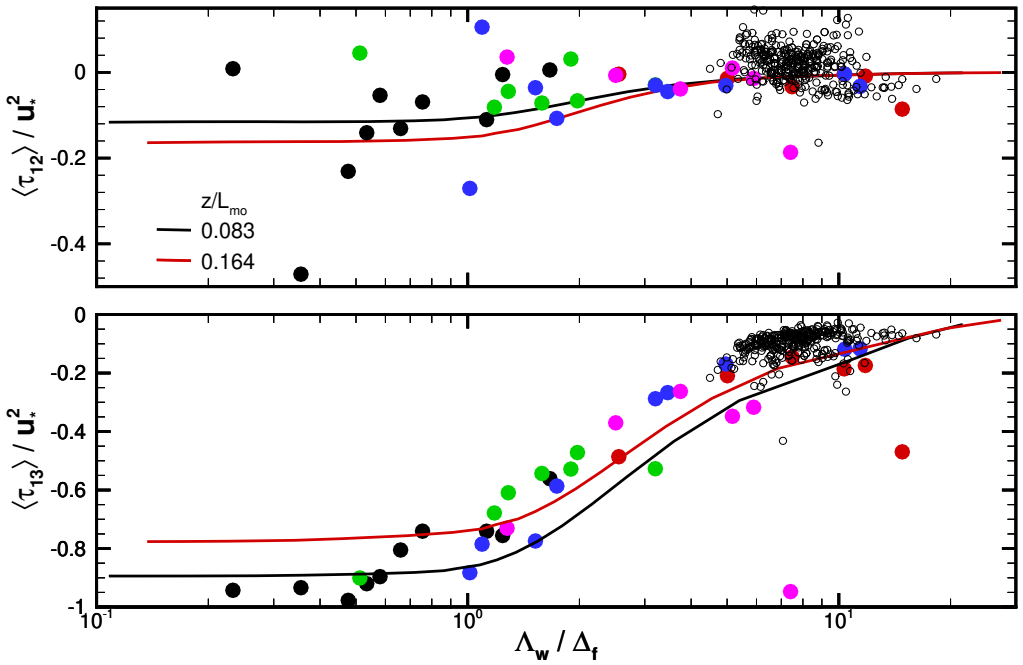

Figure 13. Variation of subfilter-scale momentum fluxes with varying resolution ratio $\Lambda_w/\triangle_f$. Horizontal momentum flux $\langle u'v'\rangle_{sfs}/u_*^2$ (upper panel) and vertical momentum flux $\langle u'w'\rangle_{sfs}/u_*^2$ (lower panel). Measurements are collected in the atmospheric surface layer over land (colored bullets) and ocean (open circles) [37,46]. The (red, black) lines show filtered results from simulation C2 with mesh 2048^3 and spacing $\triangle = 0.2\,\mathrm{m}$. The (red, black) lines are in the surface layer $z/L_{mo} = (0.164, 0.083)$ respectively. Note the different vertical scale in the upper and lower panels.

shows non-zero values of horizontal momentum flux $\langle\tau_{12}\rangle$, while the measurement scatter is too great to confidently assess this.

The horizontal and vertical scalar fluxes $\langle\tau_{1\theta}, \tau_{3\theta}\rangle$ are interesting. These SFS fluxes from LES, are in good agreement with the observations. Notice as $\Lambda_w/\triangle_f \to 0$ the vertical scalar flux tends to the surface flux Q_* as expected while the horizontal scalar flux tends to -2.5, which agrees very well with the HATS observations and also with the classic Kansas results, where Wyngaard *et al.* [62] find the ensemble average of the total scalar flux $-\langle u'\theta'\rangle/\langle w'\theta'\rangle \approx 2.5$ at large positive values of the stability parameter $z/L_{mo} \sim 0.6$. Based on the equations for scalar flux, Wyngaard [60] points out that $\langle\tau_{1\theta}\rangle$ is produced by tilting of the vertical scalar flux by vertical shear $\partial_z\langle u\rangle$ not by a horizontal gradient $\partial_x\langle\theta\rangle$, *i.e.*, an eddy viscosity model is inadequate for horizontal scalar flux when $\Lambda_w/\triangle_f$ is small. Dynamically, the tilted vortices in Fig. 9 are the agent producing horizontal scalar flux as discussed in [21].

The average SFS variances and fluxes from LES agree well with the HATS and OHATS observations over a wide range of $\Lambda_w/\triangle_f$, and thus we expect the instantaneous spatially varying SFS motions from LES are also representative of atmospheric surface layer flows. The visualization in Figs. 15, 16, and 17 show vertical momentum flux and vertical and horizontal temperature flux in horizontal planes at level $z/L_{mo} = 0.164\,\mathrm{m}$ for resolution ratios $\Lambda_f/\triangle_f = (0.15, 0.91, 2.09, 10.4)$, *i.e.*, spanning either side of the gray zone. Inspection of the figures shows a smooth transition with varying $\Lambda_w/\triangle_f$. A parameterization needs to model all of the flux when $\Lambda_w/\triangle_f$ is small and stochastic fluctuations at large $\Lambda_w/\triangle_f$. In the intermediate gray zone the SFS motions contain a fraction of the total flux, see Fig. 13, but stochastic fluctuations are also clearly present at the same time, *e.g.*, see the visualization in Fig. 15.

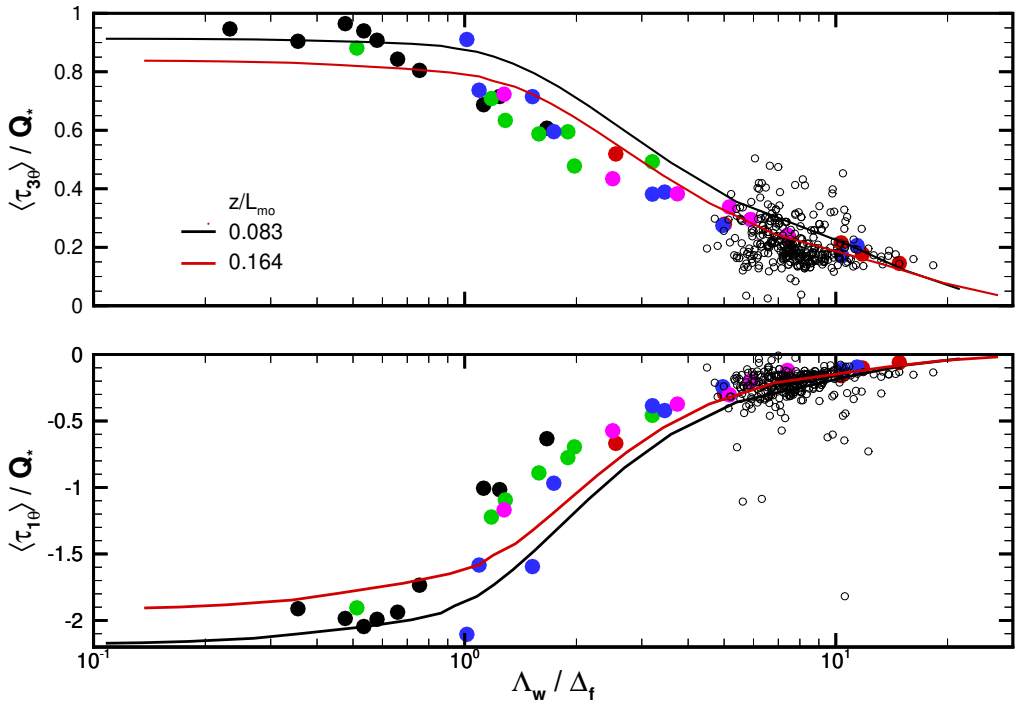

Figure 14. Variation of subfilter-scale temperature fluxes with varying resolution ratio $\Lambda_w/\triangle_f$. Horizontal flux $\langle u'\theta'\rangle_{sfs}/Q_*$ (upper panel) and vertical flux $\langle w'\theta'\rangle_{sfs}/Q_*$ (lower panel). Measurements are collected in the atmospheric surface layer over land (colored bullets) and over the ocean (open circles) [37,46]. The (red, black) lines show the filtered results from simulation C2 with mesh 2048^3. The (red, black) lines are in the surface layer $z/L_{mo} = (0.164, 0.083)$ respectively.

In the gray zone, to ensure the proper energy transfer between resolved and subgrid fields, a SFS flux parameterization needs to account for a fraction of the net flux plus fluctuations correlated with the fluctuating strain rate. To illustrate the idea consider the energy equation for the resolved motions which contains the transfer term $\tau_{ij}S_{ij}$ where S_{ij} is the resolved rate of strain tensor; recall this term also appears in the SFS energy equation with opposite sign [*e.g.*, 63]. Decomposing the SFS flux and resolved rate of strain tensors into a mean and fluctuation yields the expression,

$$\langle \tau_{ij}S_{ij}\rangle \;=\; \langle \tau_{ij}\rangle\langle S_{ij}\rangle \;+\; \langle \tau'_{ij}S'_{ij}\rangle\,; \tag{5}$$

notice $\tau'_{ij}S'_{ij}$ allows both forward and backward (backscatter) of energy which was observed in HATS [37]. Inspection of (5) shows the difficulty: energy transfer at small and large $\Lambda_w/\triangle_f$ is $\langle \tau_{ij}\rangle\langle S_{ij}\rangle$ or the turbulent correlation $\langle \tau'_{ij}S'_{ij}\rangle$, respectively. However, Fig. 18 shows that in the intermediate gray zone both terms on the right-hand-side of (5) contribute to the energy transfer. Thus a SFS flux parameterization needs to account for a fraction of the net flux but also important stochastic fluctuations because of the energy transfer between resolved and subgrid fields. The SFS momentum fluctuations are not random noise but are clearly correlated with fluctuations in strain rate. The transfer of scalar variance faces a similar dilemma in the gray zone.

Parameterizations in the gray zone are further confronted by possible "double counting" of momentum and temperature fluxes. This can result when a SFS paramterization is used outside its design range in the space $\Lambda_w/\triangle_f$. For example, this can occur in the gray zone $\Lambda_w/\triangle_f \sim 1$ when a single column model, designed for RANS vertical flux, is used at the same time the model grid resolution is sufficient to support resolved turbulence. Under these conditions the estimate of flux can be double counted [59]. Flux double counting spoils the energy and scalar transfer between the resolved and SFS fields.

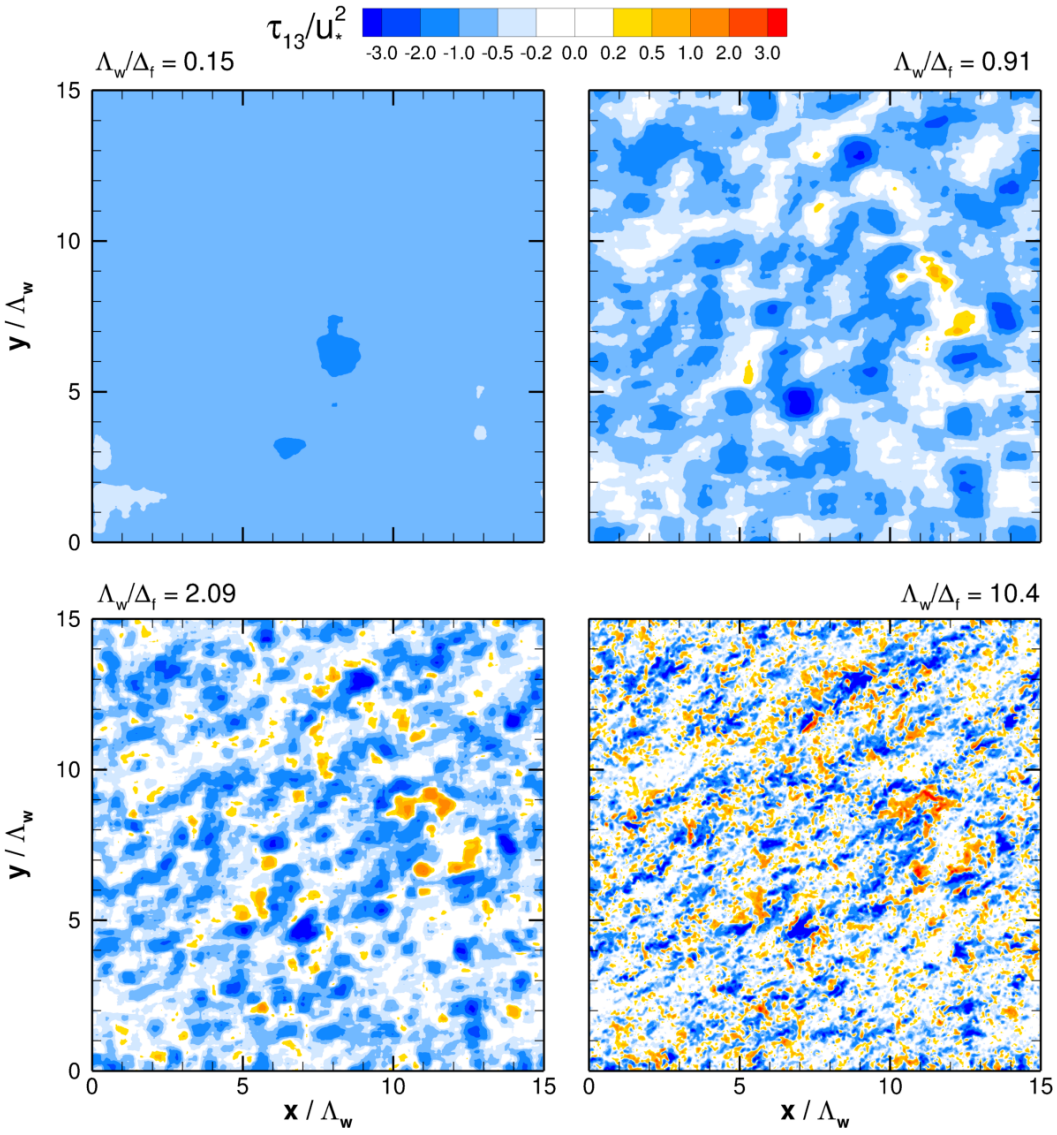

Figure 15. Subfilter-scale momentum flux τ_{13} at $z/L_{mo} = 0.164$ m with varying resolution ratio $\Lambda_w/\triangle_f = (0.52, 10.4)$, left and right panels, respectively, from simulation C2. The normalization is by u_*^2

A cursory inspection of the patterns in τ_{13} (Fig. 15) and $\tau_{3\theta}$ (Fig. 16) suggests a possible amplitude correlation, *i.e.*, $\tau_{3\theta}$ is approximately related to τ_{13} by a constant [64]. The assumption that the scalar diffusivity and momentum eddy viscosity are related is routinely adopted by LES models. The visualization of the streamwise scalar flux shows a near zero mean and small fluctuations at large $\Lambda_w/\triangle_f$; $\tau_{1\theta}$ is routinely neglected in SFS modeling [65]. At small $\Lambda_w/\triangle_f$ the horizontal scalar flux is clearly non-zero, but its impact disappears under the usual assumption of a periodic horizontally homogeneous flow $\partial_x\langle u'\theta'\rangle = 0$.

The fine mesh LES results can also be used to craft parameterizations that span the gray zone. For example, consider a $q^2 - \ell$ second-order closure that uses a prognostic equation for the unresolved SFS turbulence kinetic energy $q^2 = (u'^2 + v'^2 + w'^2)/2$ with ℓ a prescribed length scale. This closure uses a TKE equation with a model for viscous dissipation ϵ [64], typically of the form

$$\epsilon = \frac{q^3}{L_\epsilon}\,. \tag{6}$$

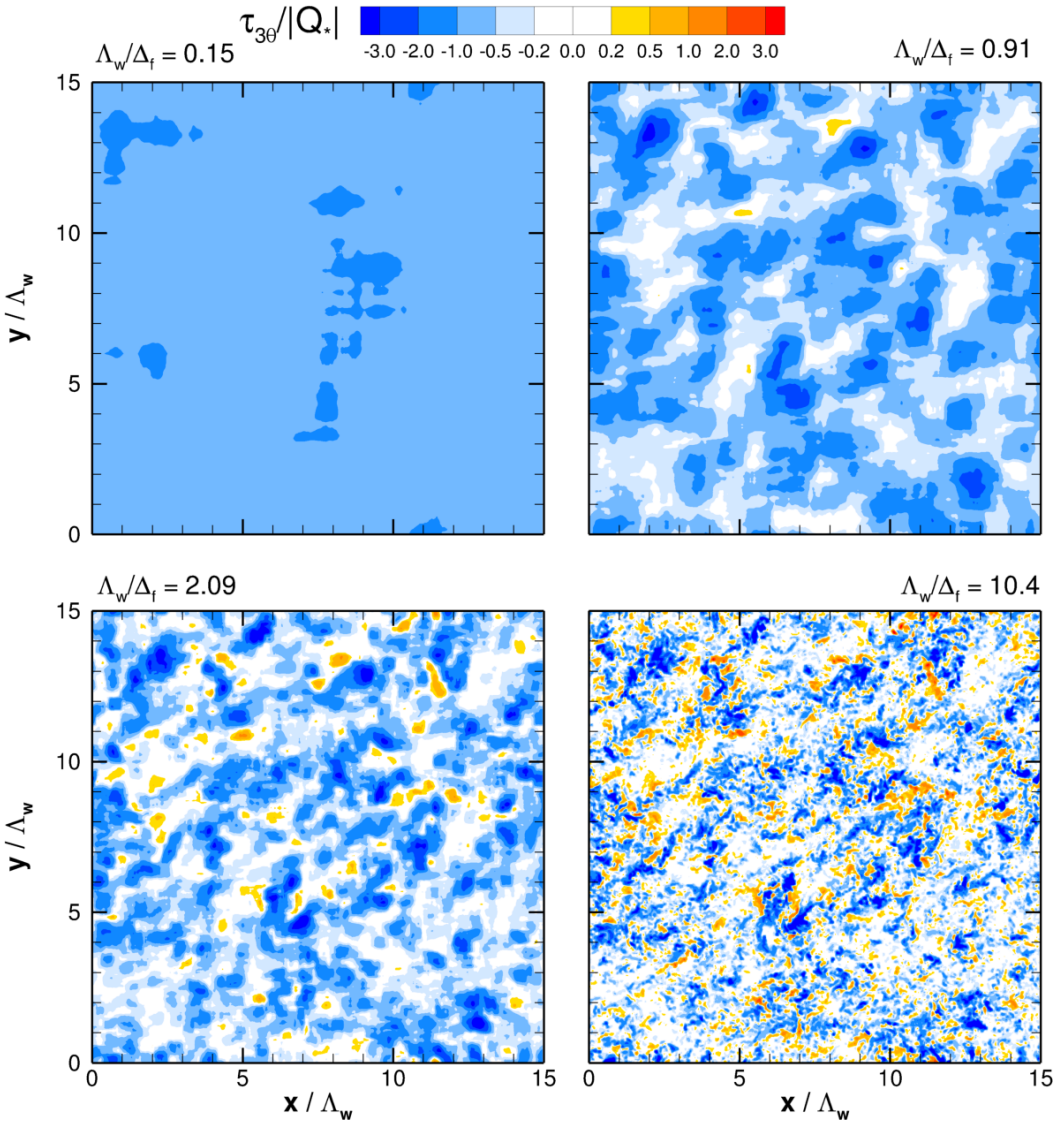

Figure 16. Subfilter-scale vertical temperature flux $\tau_{3\theta}/Q_*|$ at $z/L_{mo} = 0.164$ with varying resolution ratio $\Lambda_w/\triangle_f = ((0.15, 0.91, 2.09, 10.4))$, left and right panels, respectively, from simulation C2. To preserve the sign of the flux the normalization is by $|Q_*|$.

The dissipation model requires specification of the length scale L_ϵ. Figure 19 shows the variation of L_ϵ with inverse resolution ratio $\triangle_f/\Lambda_w$ computed from the LES results; this result is obtained by assuming constant dissipation across $\triangle_f$. For small filter widths in the LES regime q^2 is a small fraction of the total energy and $L_\epsilon \propto \triangle_f$. At large filter widths approaching the RANS regime q^2 is the total kinetic energy and the length scale saturates, *i.e.*, $L_\epsilon/\Lambda_w \sim 1.4$ in the surface layer. A smooth variation of L_ϵ is found at intermediate filter widths between the RANS and LES limits. In the middle of the gray zone $L_\epsilon \sim \Lambda_w$ at $\triangle_f = \Lambda_w$. Thus in general one needs an adaptive parameterization $L_\epsilon = L_\epsilon(z, \triangle_f/\Lambda_w)$ as the filter width varies across the RANS to LES regimes.

6. Summary and discussion

Recent high resolution large-eddy simulations (LES) of a stable atmospheric boundary layer (SBL) with mesh sizes $N = (512^3, 1024^3, 2048^3)$, or mesh spacings $\triangle = (0.78, 0.39, 0.2)$ m, are described and analyzed. The SBL posing is the GABLS1 intercomparison case for LES driven by a constant surface cooling rate $C_r = 0.25\,\mathrm{K\,hr^{-1}}$ described by Beare *et al.* [24] and Holtslag [23]. An SBL with nearly four times stronger stratification on a mesh with

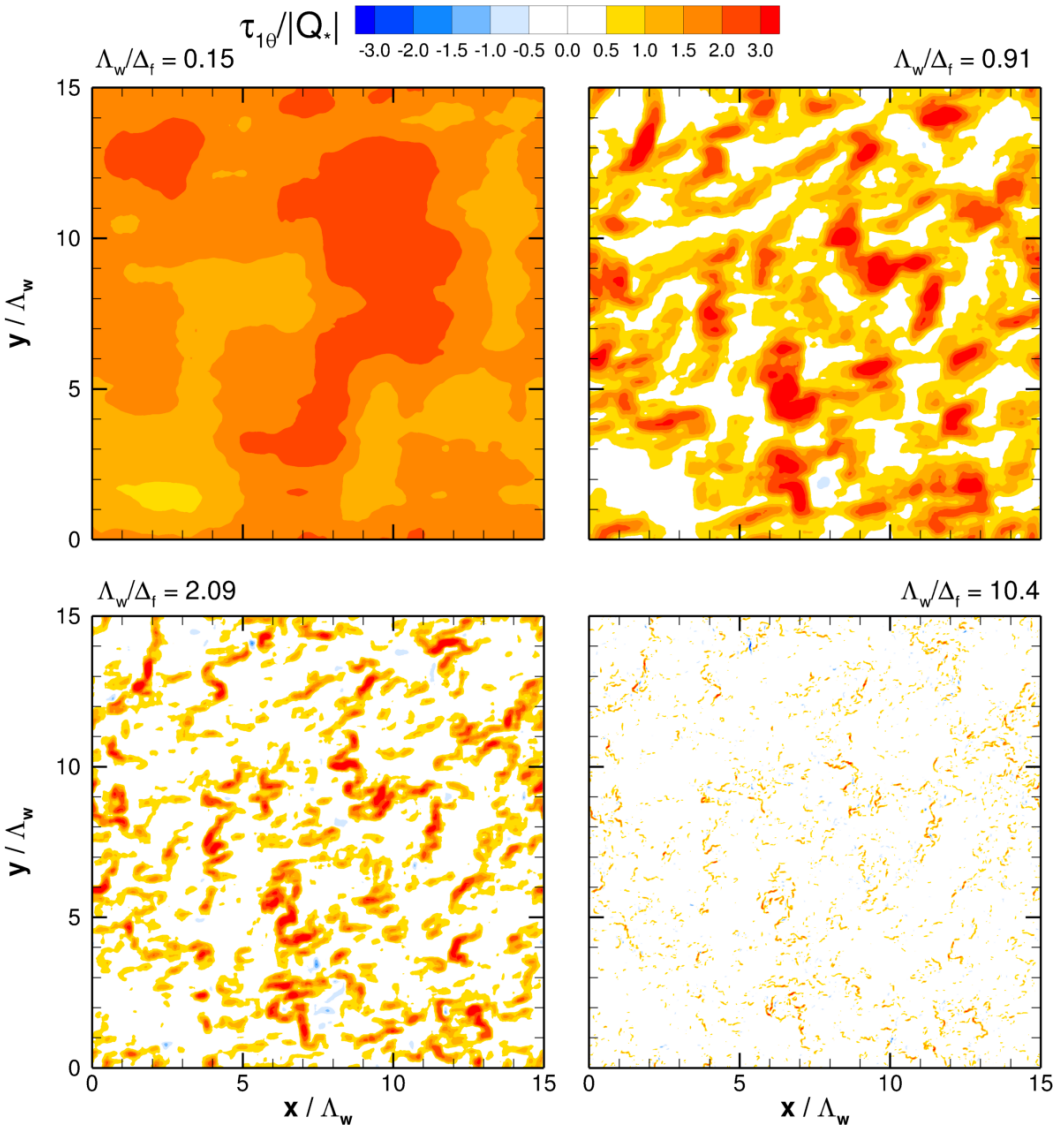

Figure 17. Subfilter-scale horizontal temperature flux $\tau_{1\theta}/|Q_*|$ at $z/L_{mo} = 0.164$ with varying resolution ratio $\Lambda_w/\triangle_f = (0.52, 10.4)$, left and right panels, respectively, from simulation C2. To preserve the sign of the flux the normalization is by $|Q_*|$.

$N = 2048^3$ is also analyzed. These recent high-resolution datasets with 2048^3 mesh points are being added to the Johns Hopkins University Turbulence Database (JHTDB) for further analysis by the research community.

The LES solutions on meshes $N = (512^3, 1024^3, 2048^3)$ are judged converged based on the good collapse of vertical profiles of mean winds, temperature, and low-order turbulence moments, *i.e.*, fluxes and variances. The largest discrepancy is in the stably stratified region above the low-level jet (LLJ) where the turbulence is small-scale and weak. The boundary-layer height between the simulations varies by less than 10% which induces small changes in friction velocity and surface temperature flux. These comparisons with different N indicate that further convergence of low-order moments is likely with even larger values. With increasing stratification, $C_r = 1\,\mathrm{K\,hr^{-1}}$, the LLJ descends and the SBL is nearly equally split into two vertical layers. Above the LLJ the Richardson number is uniform $Ri \sim 0.2$ which supports only weak turbulence.

Flow visualization shows the SBL is filled with ubiquitous temperature fronts tilted in the streamwise direction. The spatial distance separating the warm-cold fronts is thin, *i.e.*, the fronts are very sharp. Mesh refinement decreases the spatial separation between the

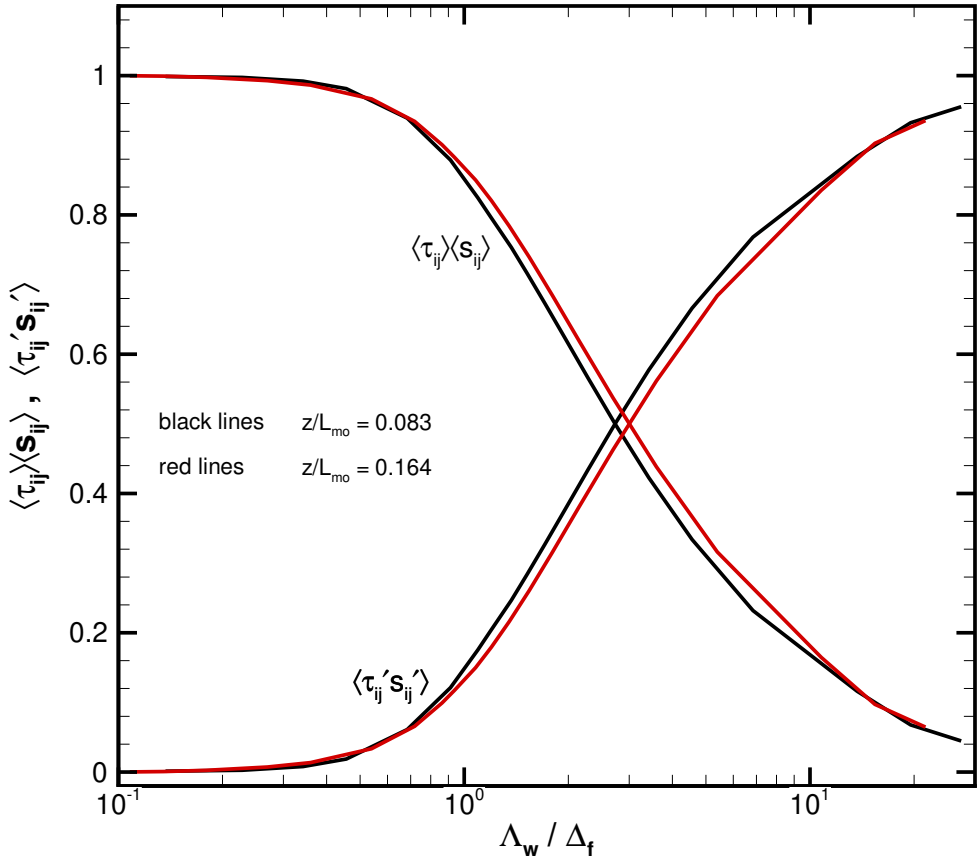

Figure 18. Variation of the production terms in Eq (5) for varying filter width $\triangle_f$ at two heights near the surface $z/L_{mo} = (0.083, 0.164)$ denoted by (black, red) lines, respectively, from simulation C2. The individual production terms are normalized by the total production $\langle\tau_{ij}S_{ij}\rangle$ at each filter width. Total production $\langle\tau_{ij}S_{ij}\rangle$ is nearly constant with varying $\triangle_f$, but slopes downward at small filter widths because of the actual subgrid model used in the LES.

fronts, and increasing stratification causes the fronts to tilt farther forward in a shallower SBL. At a fixed horizontal location x-y a temperature profile exhibits a staircase pattern in the vertical direction where sharp jumps are separated by a nearly uniform (constant) temperature. The flow visualization highlights SBL dynamics across scales. Pairs of counter-rotating, well-resolved, "horseshoe" vortices, tilted in the downstream-upward direction, are the agents inducing the sharp temperature fronts; the vortices induce both vertical and horizontal temperature and momentum fluxes. The scale of the vortices coincides with the scale of the peak in the θ and w spectra as shown by Sullivan *et al.* [21].

Subfilter-scale (SFS) motions deduced from the LES solutions are compared with observations from the horizontal array turbulence study (HATS) and the ocean horizontal turbulence study (OHATS); these multi-point measurements were collected from cross-wind arrays of sonic anemometers in the atmospheric surface layer over a range of wind speeds, stratification, and sensor spacings. The SFS momentum and temperature fluxes, $\tau_{ij} = \widehat{u_i u_j} - \widehat{u}_i\widehat{u}_j$ and $\tau_{i\theta} = \widehat{u_i\theta} - \widehat{u}_i\widehat{\theta}$, are constructed from the observations and LES using similar 2-D low-pass filters with varying filter width $\triangle_f$. Their comparisons are done using a dimensionless resolution ratio $\Lambda_w/\triangle_f$, where Λ_w is the characteristic length scale of the energy containing eddies for vertical velocity w. Over the range $0.1 < \Lambda_w/\triangle_f < 10$, the SFS fluxes and variances from the fine-mesh LES and observations are in good agreement.

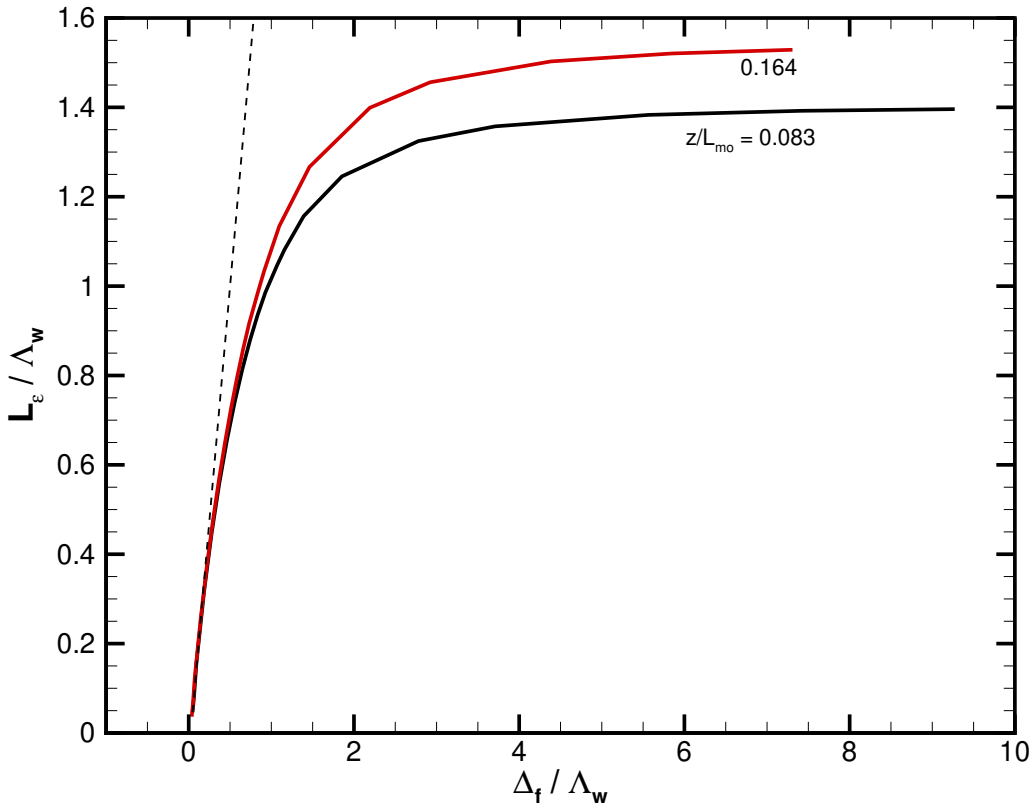

Figure 19. Variation of the dissipation length scale L_ϵ for varying filter width $\triangle_f$ at two heights near the surface $z/L_{mo} = (0.083, 0.164)$ denoted by (black, red) lines, respectively, from simulation C2. The black dashed line is a linear fit to L_ϵ for small filter widths similar to the predictions by Wyngaard [60].

At first blush this seems surprising, but notice when $\triangle_f \gg \triangle$ very well resolved turbulent motions are used to compute SFS variances and fluxes.

The limits $\Lambda_w/\triangle_f > 10$ and $\Lambda_w/\triangle_f < 0.1$ correspond to LES and unsteady Reynolds-Averaged Navier Stokes (RANS) regimes, respectively. The intermediate regime is encountered near walls and in simulations with coarse LES grids or fine mesoscale grids. The regime with $\Lambda_w/\triangle_f \sim 1$ is termed "Terra Incognita" or gray scale by Wyngaard [1]. The SFS fluxes from HATS and LES both vary smoothly across the gray scale. The SFS parameterization in the gray scale with partially resolved flux needs to account for both a "RANS" flux in addition to fluctuations. Fluctuations in SFS momentum fluxes are not random noise but are well correlated with the strain rate. A scale-aware parameterization needs to set the proper energy or scalar transfer between resolved and subgrid fields.

The good agreement between the LES results and observations is encouraging and allows fine mesh LES fields to be used for guidance in formulating SFS models and for *a priori* tests for the SBL and other high Reynolds number flows. These would be more relevant than similar tests with DNS that are limited to geophysically unrealistically low values of Reynolds number. Given the large number of SFS parameterization models that have been proposed and the several canonical geophysical flow regimes, it would be a substantial enterprise to make systematic tests, but well worthwhile. Also, in the spirit of our age, one could ask whether artificial intelligence algorithms should supervise the tests or even search beyond present SFS proposals.

7. Whither turbulence?

This section title is shamelessly borrowed from Lumley [66] which is a collection of essays about the state and direction of turbulence research at that time. (See also the biographical discussion of Lumley's life and views in Leibovich and Warhaft [67].)

Turbulent flows are ubiquitous in natural fluids, and their science is centuries old. It is an unusual science in several ways. Its governing partial differential equation, Navier-Stokes, is known and seems to be valid after many experimental tests. Yet its mathematical nature is still incompletely characterized (*n.b.*, the unclaimed Clay Mathematics Institute Millennium Prize for proof of existence and smoothness of its solutions). It is highly accessible to measurements in laboratories and Earth's atmosphere and ocean. Yet these measurements always seem to be insufficiently complete. It has been and continues to be a premier computational problem with various discrete approximations to the known continuum equations. Yet solution convergence remains elusive in pursuit of the very large Reynolds numbers in natural flows, and turbulence seems to have an endless variety of outcomes in different physical regimes. And we remember Horace Lamb's quip about whether we would even understand the nature of turbulence if it were explained to us in heaven [68].

So, we just keep plugging away. Turbulence is far too important to abandon, and measurements and simulations can always answer whatever a well-conceived next question is. We can continue to make models of how turbulence behaves in the subgrid-scale regime at high Reynolds number; they are at least useful, if not provably correct, and they are falsifiable with a next set of measurements and simulations. The solutions in this paper could play such a role for many extant models. The goal is to identify and solve problems that enable us to infer generic behaviors recognizing that many different paradigms are needed for geophysical turbulence.

The present paper is a happy confluence of multi-point atmospheric measurements, apparently adequate subgrid parameterizations, and large computational grids that takes yet another step up the tall ladder toward heaven, where maybe we'll meet Jack again.

Author Contributions: All authors contributed to the work. JCM wrote critical sections of the manuscript, suggested analysis, and edited the manuscript. CM participated in HATS, edited the manuscript, and suggested analysis. EGP ran simulations, edited the manuscript, and suggested analysis. PPS participated in HATS and OHATS, ran simulations, analyzed the observational and simulation data, and wrote large sections of the manuscript.

Funding: CM, EGP and PPS were supported by NSF award number 2103874 with the JHU to NCAR subaward 2005117865. PPS and JCM were supported by the Office of Naval Research through the Physical Oceanography Program award numbers N00014-17-1-2334 and N00014-18-1-2599, and by the National Oceanic and Atmospheric Administration award number NA19OAR4310378. PPS and EGP acknowledge support from the National Science Foundation and the Geophysical Turbulence Program at the National Center for Atmospheric Research (NCAR). We also acknowledge high-performance computing support from Cheyenne (https://doi.org/10.5065/D6RX99HX) provided by NCAR's Computational and Information Systems Laboratory, sponsored by the National Science Foundation.

Data Availability Statement: The numerical simulation data used in this manuscript will be accessible via the Johns Hopkins Turbulence Database: https://turbulence.pha.jhu.edu. The HATS and OHATS data can be accessed at https://doi.org/10.5065/D6X34VWV and https://doi.org/10.5065/D6959G0N, respectively.

Acknowledgments: The authors thank James Edson (Woods Hole Oceanographic Institute), John Wyngaard (Pennsylvanian State University) and Thomas Horst (NCAR) for their participation in the OHATS field campaign. The five reviewers provided useful comments that improved the manuscript.

Conflicts of Interest: The authors declare no conflict of interest. The funders had no role in the design of the study; in the collection, analyses, or interpretation of data; in the writing of the manuscript; or in the decision to publish the results.

References

1. Wyngaard, J.C. Toward numerical modeling in the Terra Incognita. *J. Atmos. Sci.* **2004**, *61*, 1816–1826. https://doi.org/10.1175/1520-0469(2004)061<1816:TNMITT>2.0.CO;2.
2. Patterson, G.; Orszag, S. Spectral calculations of isotropic turbulence: Efficient removal of aliasing interactions. *Phys. Fluids* **1971**, *14*, 2538. https://doi.org/10.1063/1.1693365.
3. Herring, J.R.; McWilliams, J.C. Lecture Notes on Turbulence. In *Lecture Notes from the NCAR-GTP Summer School*; Herring, J.R.; McWilliams, J.C., Eds.; World Scientific, Singapore, 1989; p. 371. https://doi.org/10.1142/0776.
4. Fernando, H.J.S. Turbulent mixing in stratified fluids. *Annu. Rev. Fluid Mech.* **1991**, *23*, 455–493. https://doi.org/10.1146/annurev.fl.23.010191.002323.
5. Fernando, H.J.S.; Weil, J.C. Whither the stable boundary layer? A shift in the research agenda. *Bull. Amer. Meteorol. Soc.* **2010**, *91*, 1475–1481. https://doi.org/10.1175/2010BAMS2770.1.
6. Mahrt, L. Stably stratified atmospheric boundary layers. *Annu. Rev. Fluid Mech.* **2014**, *46*, 23–45. https://doi.org/10.1146/annurev-fluid-010313-141354.
7. Caulfield, C.P. Layering, instabilities, and mixing in turbulent stratified flows. *Annu. Rev. Fluid Mech.* **2021**, *53*, 113–145. https://doi.org/10.1146/annurev-fluid-042320-100458.
8. Large, W.G.; McWilliams, J.C.; Doney, S.C. Oceanic vertical mixing: A review and a model with a nonlocal boundary layer parameterization. *Rev. Geophys.* **1994**, *32*, 363–403. https://doi.org/10.1029/94RG01872.
9. McWilliams, J.C. Phenomenological hunts in two-dimensional and stably stratified turbulence. In *Atmospheric Turbulence and Mesoscale Meteorology*; Federovich, E.; Rotunno, R.; Stevens, B., Eds.; Cambridge University Press, 2004; pp. 35–49. https://doi.org/10.1017/CBO9780511735035.004.
10. Cuxart, J.; Holtslag, A.A.M.; Beare, R.J.; Bazile, E.; Beljaars, A.; Cheng, A.; Conangla, L.; Ek, M.; Freedman, F.; Hamdl, R.; et al. Single-column model intercomparison for a stably stratified atmospheric boundary layer. *Bound.-Layer Meteorol.* **2006**, *118*, 273–303. https://doi.org/10.1007/s10546-005-3780-1.
11. Svensson, G.; Holtslag, A.A.M. Analysis of model results for the turning of the wind and related momentum fluxes in the stable boundary layer. *Bound.-Layer Meteorol.* **2009**, *132*, 261–277. https://doi.org/10.1007/s10546-009-9395-1.
12. Holtslag, A.A.M.; Svensson, G.; Baas, P.; Basu, S.; Beare, B.; Beljaars, A.C.M.; Bosveld, F.C.; Cuxart, J.; Lindvall, J.; Steeneveld, G.J.; et al. Stable atmospheric boundary layers and diurnal cycles: Challenges for weather and climate models. *Bull. Amer. Meteorol. Soc.* **2013**, *94*, 1691–1706. https://doi.org/10.1175/BAMS-D-11-00187.1.
13. Heisel, M.; Sullivan, P.P.; Katul, G.G.; Chamecki, M. Turbulence organization and mean profile shapes in the stably stratified boundary layer: Zones of uniform momentum and air temperature. *Bound.-Layer Meteorol.* **2022**. https://doi.org/10.1007/s10546-022-00771-0.
14. Wyngaard, J.C.; Seaman, N.; Kimmel, S.J.; Otte, M.; Di, X.; Gilbert, K.E. Concepts, observations, and simulation of refractive index turbulence in the lower atmosphere. *Radio Science* **2001**, *36*, 643–669. https://doi.org/10.1029/2000RS002380.
15. Kelley, N.; Shirazi, M.; Buhl, M.; Jager, D.; Wilde, S.; Adams, J.; Bianchi, J.; Sullivan, P.; Patton, E. Lamar low-level jet project interim report. Technical Report NREL/TP-500-34593, National Renewable Energy Laboratory, Golden, CO, 2003. https://doi.org/10.2172/15006544.
16. Weil, J.C. Stable boundary layer modeling for air quality applications. In Proceedings of the Air Pollution Modeling and Its Application XXI; Castelli, S.T.; Steyn, D., Eds. Springer, 2012, NATO Science for Peace and Security Series C: Environmental Security, pp. 57–61. https://doi.org/10.1007/978-94-007-1359-8_10.
17. Nieuwstadt, F.T.M. Direct numerical simulation of stable channel flow at large stability. *Bound.-Layer Meteorol.* **2005**, *116*, 277–299. https://doi.org/10.1007/s10546-004-2818-0.
18. van de Wiel, B.J.H.; Moene, A.F.; Hartogensis, O.K.; de Bruin, H.A.R.; Holtslag, A.A.M. Intermittent turbulence in the stable boundary layer over land. Part III. A classification for observations during CASES-99. *J. Atmos. Sci.* **2003**, *60*, 2509–2522. https://doi.org/10.1175/1520-0469(2003)060<2509:ITITSB>2.0.CO;2.
19. van Haren, H.; Gostiaux, L. A deep-ocean Kelvin-Helmholtz billow train. *Geophys. Res. Lett.* **2010**, *37*, L03605. https://doi.org/10.1029/2009GL041890.
20. Moeng, C.H.; Sullivan, P.P. Large-eddy simulation. In *Encyclopedia of Atmospheric Sciences 2nd Edition*; North, G.R.; Zhang, F.; Pyle, J., Eds.; Academic Press, 2015; Vol. 4, pp. 232–240. https://doi.org/10.1016/B978-0-12-382225-3.00201-2.
21. Sullivan, P.P.; Weil, J.C.; Patton, E.G.; Jonker, H.J.J.; Mironov, D.V. Turbulent winds and temperature fronts in large-eddy simulations of the stable atmospheric boundary layer. *J. Atmos. Sci.* **2016**, *73*, 1815–1840. https://doi.org/10.1175/JAS-D-15-0339.1.
22. Sullivan, P.P.; McWilliams, J.C.; Moeng, C.H. A subgrid-scale model for large-eddy simulation of planetary boundary-layer flows. *Bound.-Layer Meteorol.* **1994**, *71*, 247–276. https://doi.org/10.1007/BF00713741.

23. Holtslag, A.A.M. GEWEX atmospheric boundary-layer study GABLS on stable boundary layers. *Bound.-Layer Meteorol.* **2006**, *118*, 243–246. https://doi.org/10.1007/s10546-005-9008-6.
24. Beare, R.J.; Macvean, M.K.; Holtslag, A.A.M.; Cuxart, J.; Esau, I.; Golaz, J.C.; Jimenez, M.A.; Khairoutdinov, M.; Kosovic, B.; Lewellen, D.; et al. An intercomparison of large-eddy simulations of the stable boundary layer. *Bound.-Layer Meteorol.* **2006**, *118*, 242–272. https://doi.org/10.1007/s10546-004-2820-6.
25. Huang, J.; Bou-Zeid, E. Turbulence and vertical fluxes in the stable atmospheric boundary layer. Part I: A large-eddy simulation study. *J. Atmos. Sci.* **2013**, *70*, 1513–1527. https://doi.org/10.1175/JAS-D-12-0167.1.
26. Li, Y.; Perlman, E.; Wan, M.; Yang, Y.; Meneveau, C.; Burns, R.; Chen, S.; Szalay, A.; Eyink, G. A public turbulence database cluster and applications to study Lagrangian evolution of velocity increments in turbulence. *J. Turbulence* **2008**, *9*, N31. https://doi.org/10.1080/14685240802376389.
27. Graham, J.; Kanov, K.; Yang, X.; Lee, M.; Malaya, N.; Lalescu, C.; Burns, R.; Eyink, G.; Szalay, A.; Moser, R.; et al. A web services accessible database of turbulent channel flow and its use for testing a new integral wall model for LES. *J. Turbulence* **2016**, *17*, 181–215. https://doi.org/10.1080/14685248.2015.1088656.
28. Piomelli, U.; Moin, P.; Ferziger, J.H. Model consistency in large eddy simulation of turbulent channel flows. *Phys. Fluids* **1988**, *31*, 1884–1891. https://doi.org/10.1063/1.866635.
29. Liu, S.; Meneveau, C.; Katz, J. On the properties of similarity subgrid-scale models as deduced from measurements in a turbulent jet. *J. Fluid Mech.* **1994**, *275*, 83–119. https://doi.org/10.1017/S0022112094002296.
30. Horst, T.W.; Kleissl, J.; Lenschow, D.H.; Meneveau, C.; Moeng, C.H.; Parlange, M.B.; Sullivan, P.P.; Weil, J.C. Field observations to obtain spatially-filtered turbulence fields from transverse arrays of sonic anemometers in the atmospheric surface layer. *J. Atmos. Sci.* **2004**, *61*, 1566–1581. https://doi.org/10.1175/1520-0469(2004)061<1566:HFOTOS>2.0.CO;2.
31. Meneveau, C.; Lund, T.S. The dynamic Smagorinsky model and scale-dependent coefficients in the viscous range of turbulence. *Phys. Fluids* **1997**, *9*, 3932–3934. https://doi.org/10.1063/1.869493.
32. Tong, C.; Wyngaard, J.C.; Khanna, S.; Brasseur, J.G. Resolvable- and subgrid-scale measurement in the atmospheric surface layer: Technique and issues. *J. Atmos. Sci.* **1998**, *55*, 3114–3126. https://doi.org/10.1175/1520-0469(1998)055<3114:RASSMI>2.0.CO;2.
33. Tong, C.; Wyngaard, J.C.; Brasseur, J.G. Experimental study of the subgrid-scale stresses in the atmospheric surface layer. *J. Atmos. Sci.* **1999**, *56*, 2277–2292. https://doi.org/10.1175/1520-0469(1999)056<2277:ESOTSS>2.0.CO;2.
34. Tao, B.; Katz, J.; Meneveau, C. Geometry and scale relationships in high Reynolds number turbulence determined from three-dimensional holographic velocimetry. *Phys. Fluids* **2000**, *12*, 941–944. https://doi.org/10.1063/1.870348.
35. Meneveau, C.; Katz, J. Scale-invariance and turbulence models for large-eddy simulations. *Annu. Rev. Fluid Mech.* **2000**, *32*, 1–32. https://doi.org/10.1146/annurev.fluid.32.1.1.
36. Pope, S.B. *Turbulent Flows*; Cambridge University Press, 2000; p. 771. https://doi.org/10.1017/CBO9780511840531.
37. Sullivan, P.P.; Horst, T.W.; Lenschow, D.H.; Moeng, C.H.; Weil, J.C. Structure of subfilter-scale fluxes in the atmospheric surface layer with application to large-eddy simulation modeling. *J. Fluid Mech.* **2003**, *482*, 101–139. https://doi.org/10.1017/S0022112003004099.
38. Kleissl, J.; Meneveau, C.; Parlange, M.B. On the magnitude and variability of subgrid-scale eddy-diffusion coefficients in the atmospheric surface layer. *J. Atmos. Sci.* **2003**, *60*, 2372–2388. https://doi.org/10.1175/1520-0469(2003)060<2372:OTMAVO>2.0.CO;2.
39. Kleissl, J.; Parlange, M.; Meneveau, C. Field experimental study of dynamic Smagorinsky models in the atmospheric surface layer. *J. Atmos. Sci.* **2004**, *61*, 2296–2307. https://doi.org/10.1175/1520-0469(2004)061<2296:FESODS>2.0.CO;2.
40. Chen, Q.; Tong, C. Investigation of the subgrid-scale stress and its production rate in a convective atmospheric boundary layer using measurement data. *J. Fluid Mech.* **2006**, *547*, 65–104. https://doi.org/10.1017/S0022112005007196.
41. Hatlee, S.C.; Wyngaard, J.C. Improved subfilter-scale models from the HATS field data. *J. Atmos. Sci.* **2007**, *64*, 1694–1705. https://doi.org/10.1175/JAS3909.1.
42. Chamecki, M.; van-Hout, R.; Meneveau, C.; Parlange, M.B. Concentration profiles of particles settling in the neutral and stratified atmospheric surface layer. *Bound.-Layer Meteorol.* **2007**, *125*, 25–38. https://doi.org/10.1007/s10546-007-9194-5.
43. Ramachandran, S.; Wyngaard, J.C. Subfilter-scale modelling using transport equations: Large-eddy simulation of the moderately convective atmospheric boundary layer. *Bound.-Layer Meteorol.* **2011**, *139*, 1–35. https://doi.org/10.1007/s10546-010-9571-3.
44. Higgins, C.W.; Meneveau, C.; Parlange, M.B. The effect of filter dimension on the subgrid-scale stress, heat flux, and tensor alignments in the atmospheric surface layer. *J. Atmos. Ocean. Tech.* **2007**, *24*, 360–375. https://doi.org/10.1175/JTECH1991.1.
45. Kumar, V.; Kleissl, J.; Meneveau, C.; Parlange, M.B. Large-eddy simulation of a diurnal cycle of the atmospheric boundary layer: Atmospheric stability and scaling issues. *Water Resour. Res.* **2006**, *42*. https://doi.org/10.1029/2005WR004651.
46. Sullivan, P.P.; Edson, J.B.; Horst, T.W.; Wyngaard, J.C.; Kelly, M. Subfilter scale fluxes in the marine surface layer: Results from the Ocean Horizontal Array Turbulence Study (OHATS). In Proceedings of the 17th Symposium on Boundary Layer and Turbulence; American Meteorological Society, , 2006; pp. 1–8. Paper 4.1, http://ams.confex.com/ams/BLTAgFBioA/techprogram/paper_110884.htm.
47. Bou-Zeid, E.; Higgins, C.; Huwald, H.; Meneveau, C.; Parlange, M.B. Field study of the dynamics and modelling of subgrid-scale turbulence in a stable atmospheric surface layer over a glacier. *J. Fluid Mech.* **2010**, *665*, 480–515. https://doi.org/10.1017/S0022112010004015.

48. Patton, E.G.; Horst, T.W.; Sullivan, P.P.; Lenschow, D.H.; Oncley, S.P.; Brown, W.O.J.; Burns, S.P.; Guenther, A.B.; Held, A.; Karl, T.; et al. The canopy horizontal array turbulence study. *Bull. Amer. Meteorol. Soc.* **2011**, *92*, 593–611. https://doi.org/10.1175/2010BAMS2614.1.
49. Nguyen, K.X.; Horst, T.W.; Oncley, S.P.; Tong, C. Measurements of the budgets of the subgrid-scale stress and temperature flux in the convective atmospheric surface layer. *J. Fluid Mech.* **2013**, *729*, 388–422. https://doi.org/10.1017/jfm.2013.302.
50. Chow, F.K.; Moin, P. A further study of numerical errors in large-eddy simulations. *J. Comp. Phys.* **2003**, *184*, 366–380. https://doi.org/10.1016/S0021-9991(02)00020-7.
51. Sullivan, P.P.; Patton, E.G. The effect of mesh resolution on convective boundary-layer statistics and structures generated by large-eddy simulation. *J. Atmos. Sci.* **2011**, *68*, 2395–2415. https://doi.org/10.1175/JAS-D-10-05010.1.
52. Geurts, B.J.; Fröhlich, J. A framework for predicting accuracy limitations in large-eddy simulation. *Phys. Fluids* **2002**, *14*, L41–L44. https://doi.org/10.1063/1.1480830.
53. Sullivan, P.P.; Moeng, C.H.; Stevens, B.; Lenschow, D.H.; Mayor, S.D. Structure of the entrainment zone capping the convective atmospheric boundary layer. *J. Atmos. Sci.* **1998**, *55*, 3042–3064. https://doi.org/10.1175/1520-0469(1998)055<3042:SOTEZC>2.0.CO;2.
54. Dai, Y.; Basu, S.; Maronga, B.; de Roode, S.R. Addressing the grid-size sensitivity issue in large-eddy simulations of stable boundary layers. *Bound.-Layer Meteorol.* **2021**, *178*, 63–89. https://doi.org/10.1007/s10546-020-00558-1.
55. Adrian, R.J. Stochastic estimation of the structure of turbulent fields. In *Eddy Structure Identification*; Bonnet, J.P., Ed.; Springer Verlag, 1996; pp. 145–196. https://doi.org/10.1007/978-3-7091-2676-9_3.
56. Kimura, Y.; Herring, J.R. Diffusion in stably stratified turbulence. *J. Fluid Mech.* **1996**, *328*, 253–269. https://doi.org/10.1017/S0022112096008713.
57. Kaimal, J.C.; Finnigan, J.J. *Atmospheric Boundary Layer Flows*; Oxford University Press, 1994. https://doi.org/10.1093/oso/9780195062397.001.0001.
58. Bryan, G.H.; Morrison, H. Sensitivity of a simulated squall line to horizontal resolution and parameterization of microphysics. *Mon. Wea. Rev.* **2012**, *140*, 202–225. https://doi.org/10.1175/MWR-D-11-00046.1.
59. Doubrawa, P.; Muñoz-Esparza, D. Simulating real atmospheric boundary layers at gray-zone resolutions: How do currently available turbulence parameterizations perform? *Atmosphere* **2020**, *11*, 1–19. https://doi.org/10.3390/atmos11040345.
60. Wyngaard, J.C. Changing the face of small-scale meteorology. In *Atmospheric Turbulence and Mesoscale Meteorology*; Federovich, E.; Rotunno, R.; Stevens, B., Eds.; Cambridge University Press, 2004; pp. 17–34. https://doi.org/10.1017/CBO9780511735035.003.
61. Perot, J.B.; Gadebusch, J. A self adapting turbulence model for flow simulation at any mesh resolution. *Phys. Fluids* **2007**, *19*, 115105. https://doi.org/10.1063/1.2780195.
62. Wyngaard, J.C.; Cóte, O.R.; Izumi, Y. Local free convection, similarity, and the budgets of shear stress and heat flux. *J. Atmos. Sci.* **1971**, *28*, 1171–1182. https://doi.org/10.1175/1520-0469(1971)028<1171:LFCSAT>2.0.CO;2.
63. Moeng, C.H. A large-eddy simulation model for the study of planetary boundary-layer turbulence. *J. Atmos. Sci.* **1984**, *41*, 2052–2062. https://doi.org/10.1175/1520-0469(1984)041<2052:ALESMF>2.0.CO;2.
64. Moeng, C.H.; Wyngaard, J.C. Evaluation of turbulent transport and dissipation closures in second-order modeling. *J. Atmos. Sci.* **1989**, *46*, 2311–2330. https://doi.org/10.1175/1520-0469(1989)046<2311:EOTTAD>2.0.CO;2.
65. Deardorff, J.W. Three-dimensional numerical modeling of the planetary boundary layer. In *Workshop on Micrometeorology*; Haugen, D.A., Ed.; American Meteorological Society, 1972; pp. 271–311.
66. Lumley, J.L., Ed. *Whither Turbulence? Turbulence at the Crossroads*, Vol. 357. Springer Berlin, Heidelberg, 1990. https://doi.org/10.1007/3-540-52535-1.
67. Leibovich, S.; Warhaft, Z. John Leask Lumley: Whither Turbulence? *Annu. Rev. Fluid Mech.* **2018**, *50*, 1–23. https://doi.org/10.1146/annurev-fluid-122316-044524.
68. Goldstein, S. Fluid mechanics in the first half of this century. *Annu. Rev. Fluid Mech.* **1969**, *1*, 1–29. https://doi.org/10.1146/annurev.fl.01.010169.000245.